JGR Planets

RESEARCH ARTICLE
10.1029/2019JE006015

Key Points:
- We present a method for determining the planetary tidal response using laboratory-based viscoelastic models and apply it to Mars
- Maxwellian rheology results in considerably biased (low) viscosities and should be used with caution when studying tidal dissipation
- Mars' rheology and interior structure will be further constrained from InSight measurements of tidal phase lags at distinct periods

Correspondence to:
A. Bagheri,
amirhossein.bagheri@erdw.ethz.ch

Citation:
Bagheri, A., Khan, A., Al-Attar, D., Crawford, O., & Giardini, D. (2019). Tidal response of Mars constrained from laboratory-based viscoelastic dissipation models and geophysical data. *Journal of Geophysical Research: Planets*, *124*. https://doi.org/10.1029/2019JE006015

Received 6 MAY 2019
Accepted 19 AUG 2019
Accepted article online 29 AUG 2019
Corrected 21 NOV 2019

This article was corrected on 21 NOV 2019. See the end of the full text for details.

Tidal Response of Mars Constrained From Laboratory-Based Viscoelastic Dissipation Models and Geophysical Data

A. Bagheri[1], A. Khan[1,2], D. Al-Attar[3], O. Crawford[3], and D. Giardini[1]

[1]Institute of Geophysics, ETH Zürich, Zürich, Switzerland, [2]Institute of Theoretical Physics, University of Zürich, Zürich, Switzerland, [3]Bullard Laboratories, Department of Earth Sciences, University of Cambridge, Cambridge, UK

Abstract We employ laboratory-based grain size- and temperature-sensitive rheological models to describe the viscoelastic behavior and tidal response of terrestrial bodies with focus on Mars. We consider five rheological models: Maxwell, extended Burgers, Andrade, Sundberg-Cooper, and a power law approximation. The question of which model provides the most appropriate description of dissipation in planetary bodies, remains an open issue. To examine this, we build crust and mantle models of Mars (density and elasticity) that are computed self-consistently through phase equilibrium calculations as a function of pressure, temperature, and bulk composition, whereas core properties are based on an Fe-S parameterization. We assess the compatibility of the viscoelastic models by inverting tidal response, mean density, and moment of inertia of Mars for its thermal, elastic, and attenuation structure. Our results show that although all viscoelastic models fit the data, (1) their predictions of the tidal response at other periods and harmonic degrees are distinct, implying that our approach can be used to distinguish between the various models from seismic and/or tidal observations (e.g., with InSight), and (2) Maxwell is only capable of fitting data for unrealistically low viscosities. All viscoelastic models converge upon similar interior structure models: large liquid cores (1,750–1,890 km in radius) that contain 17–20.5 wt% S and, consequently, no silicate perovskite-dominated lower mantle. Finally, the methodology proposed here is generally formulated and applicable to other solar and extrasolar system bodies where the study of tidal dissipation presents an important means for determining interior structure.

Plain Language Summary A planet responds to tidal forces, such as those created by an orbiting moon, by deforming, which causes changes in its gravitational potential field. If the body responds elastically, the tide raised on the planet by its moon aligns with the tide-raising potential, as a result of which no energy dissipation within the planet occurs. However, ordinary planetary materials respond anelastically, which means that energy is dissipated and, consequently, the bulge is misaligned with the tide-raising moon. The induced deformation of the body due to an external force depends on its interior structure such that rigid bodies do not deform appreciably, whereas less rigid bodies deform significantly. Here, we use observations for the Mars-Phobos system to constrain Mars's interior. Models that describe the planet's response to an external force are based on laboratory measurements of the deformation of major planetary materials. We conclude that Mars has a relatively large liquid iron core containing abundant amounts of sulfur as light alloying element. The Mars InSight mission will make further measurements of the planet's tidal response for comparison with our results, which will improve our understanding of Mars's interior structure and dynamical evolution.

1. Introduction

A planet responds to tidal forces by deforming, which causes a change in its gravitational potential field (see Figure 1). If the response is purely elastic, the tide raised on the planet by its moon, and vice versa, will be aligned with the tide-raising potential, as a result of which the orbit of the moon will be unaffected; that is, there is no torque acting and no dissipation occurs within either body. If, however, the planet reacts anelastically, dissipation is acting, and the tidal bulge and the tide-raising potential are misaligned. Since the tidal bulge reacts by applying a torque, which is proportional to the amplitude of the tide and to the sine of the tidal

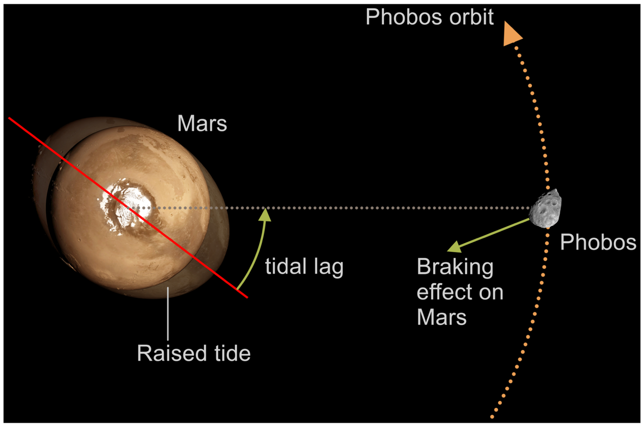

Figure 1. Illustration of the tidal interaction between Mars and its larger moon Phobos. Courtesy of David Ducros/IPGP.

lag angle or phase lag, the orbit of the moon changes. Consequently, the phase lag, which is a measure of tidal dissipation, is determined from the angle between the tide-raising force and the tide itself, and depends on the anelastic structure, whereas the amplitude of the tidal response is mostly sensitive to the elastic structure. Thus, by measuring orbital changes of natural or artificial satellites around planets or landed spacecraft, information on a planet's interior structure can be derived as has been done for the terrestrial solar system planets and the Moon (e.g., Bills et al., 2005; Dumoulin et al., 2017; Efroimsky & Lainey, 2007; Hauck et al., 2013; Khan & Connolly, 2008; Khan et al., 2018; Konopliv & Yoder, 1996; Nimmo & Faul, 2013; Nimmo et al., 2012; Padovan et al., 2013; Rivoldini et al., 2011; Williams et al., 2006; Williams & Boggs, 2015; Williams et al., 2014; Yoder, 1995; Yoder et al., 2003; Zharkov & Gudkova, 2005, among others).

The anelastic processes that most solid state materials undergo in response to a forcing are governed by dissipative processes at the microscopic scale, in particular, viscoelastic relaxation of the shear modulus due to elastically accommodated and dislocation- and diffusion-assisted grain boundary sliding (Faul & Jackson, 2015; Karato & Spetzler, 1990; Karato et al., 2015; Ranalli, 2001; Takei et al., 2014). Several models have been proposed to describe the viscoelastic behavior of planetary materials. For example, Maxwell's model, the simplest of all rheological models, has often been called upon when studying tidal dissipation in planets and moons (e.g., Bills et al., 2005; Correia et al., 2014; Efroimsky & Lainey, 2007; Remus et al., 2012). Yet this model only includes an elastic and a viscous response without a transient regime that, from a timescale point of view, covers most of the period range of interest where tidal dissipation actually occurs. Also, Maxwell's model has difficulty in reproducing the observed frequency dependence of dissipation $\propto\omega^{-\alpha}$, where ω is the angular frequency and α the frequency exponent (e.g., Benjamin et al., 2006; Jackson et al., 2002; Minster & Anderson, 1981). As a consequence, Maxwellian rheology results in an unsatisfactory explanation for the tidal response of planetary bodies like Mars, the Moon, and the Earth (Bills et al., 2005; Castillo-Rogez et al., 2011; Lau & Faul, 2019; Nimmo & Faul, 2013; Nimmo et al., 2012; Renaud & Henning, 2018; Williams & Boggs, 2015).

In response hereto, more complex grain size- and temperature-dependent models have been proposed. Among these figure the models of Andrade, Burgers, Sundberg-Cooper, and power law approximation scheme, which have been studied experimentally (Jackson & Faul, 2010; Jackson et al., 2002; McCarthy et al., 2011; Sasaki et al., 2019; Sundberg & Cooper, 2010; Takei et al., 2014). Laboratory experiments of torsional forced oscillation data on anhydrous melt-free olivine appear to favor the extended Burgers model over other rheological models because of its ability to describe the transition from (anharmonic) elasticity to grain size-sensitive viscoelastic behavior (Faul & Jackson, 2015). Because of the improved flexibility that comes with a larger number of degrees of freedom, application of these laboratory-based dissipation models to geophysical problems has nonetheless resulted in considerable improvement in matching the observed frequency dependence of dissipation, in addition to simultaneously fitting attenuation-related data that span the frequency range from the dominant seismic wave period (~1 s) over normal modes (~1 hr) to the very long-period tides (~20 years), that is, a frequency range spanning 5 orders of magnitude (Benjamin et al., 2006; Efroimsky, 2012a, 2012b; Henning et al., 2009; Khan et al., 2018; Lau & Faul, 2019; Nimmo & Faul, 2013; Nimmo et al., 2012; Renaud & Henning, 2018).

While qualitatively similar in that the various viscoelastic models can be described in terms of dashpot and spring elements that are arranged in series and in parallel, it is yet to be understood to what extent these models are quantitatively similar on planetary scales, that is, are capable of making predictions that match global geophysical observations at different forcing frequencies for a set of realistic models of the interior structure of planets. While most studies focus on application of a single viscoelastic dissipation model to solar system objects, like Mercury (Padovan et al., 2013), Venus (Dumoulin et al., 2017), Earth (Abers et al., 2014; Agnew, 2015; Bellis & Holtzman, 2014; Karato et al., 2015; Lau & Faul, 2019), the Moon (Efroimsky, 2012a, 2012b; Harada et al., 2014; Karato, 2013; Nimmo et al., 2012; Qin et al., 2016; Williams & Boggs, 2015), Mars (Bills et al., 2005; Efroimsky & Lainey, 2007; Khan et al., 2018; Lognonné & Mosser, 1993; Nimmo & Faul, 2013; Sohl & Spohn, 1997; Yoder et al., 2003; Zharkov & Gudkova, 2005), Io (Bierson & Nimmo, 2016; Renaud & Henning, 2018; Hussmann & Spohn, 2004), Iapetus (Peale, 1977; Robuchon et al., 2010; Castillo-Rogez et al., 2011), Europa (Moore & Schubert, 2000; Hussmann & Spohn, 2004; Wahr et al., 2009; A et al., 2014), Ganymede (A et al., 2014; Kamata et al., 2016), Enceladus (Choblet et al., 2017; Roberts & Nimmo, 2008), and exoplanets (Efroimsky, 2012b; Henning et al., 2009; Renaud & Henning, 2018), studies that quantitatively investigate several viscoelastic models concomitantly by formulating the problem in a geophysical inverse sense have yet to be undertaken.

With this in mind, we consider a series of laboratory-based viscoelastic dissipation models and quantitatively compare them using geophysical inversion with the purpose of constraining attenuation properties of planets from seismic to tidal timescales. Here, we focus on Mars for which the tidal response due to Phobos (amplitude and phase lag), in addition to mean density and mean moment of inertia, are available. The approach adopted here builds upon and extends previous work (e.g., Castillo-Rogez et al., 2011; Khan et al., 2018; Renaud & Henning, 2018) in that it seeks to combine a suite of experimentally constrained grain size-, temperature-, and frequency-dependent viscoelastic models (Andrade, extended Burgers, Sundberg-Cooper, Maxwell, and a power law approximation scheme) with petrologic phase equilibrium computations that enable self-consistent computation of geophysical responses for direct comparison to observations. The advantage of this approach is that it anchors internal structure parameters that are in laboratory-based models, while geophysical inverse methods are simultaneously employed to optimize profiles of, seismic wave speeds, dissipation, and density to match a set of geophysical observations.

Predictions of, for example, the tidal response at different periods can be made and tested against results that are expected to be obtained from NASA's Mars InSight (Interior Exploration using Seismic Investigations, Geodesy and Heat Transport) mission, which has been operating on Mars for 8 months since its deployment. InSight will measure attenuation, with both the SEIS (Seismic Experiment for Internal Structure; Lognonné, 2019) and RISE (Rotation and Interior Structure Experiment; Folkner et al., 2018) instruments at periods ranging from seconds (seismic events) to months (nutation and precession of Mars's rotation axis). The observation of attenuation at periods other than the main Phobos tide provides a means for distinguishing between the various laboratory-based dissipation models and will turn out to be of particular importance for understanding the thermal and viscoelastic behavior of Mars. For community use, we tabulated predicted model responses (Love numbers and attenuation) at a number of distinct periods and spherical harmonic degrees for each of the rheological models considered here. Finally, we would like to note that although this study focuses on Mars, the methodology described herein is generally applicable and is easily extendable to other solar system bodies and beyond.

2. Background

2.1. Geophysical Analysis

The tidal bulge raised on Mars (see Figure 1) due to its orbiting moon Phobos, is a function of its internal structure and the forcing itself. Because dissipation is acting, the bulge does not align with the barycenteric axis (defined as the line that extends between the center of masses of the two objects and indicated by the dashed line in Figure 1) but is lagging behind Phobos. As a result of the tidal bulge, changes in the potential field and deformations in both radial and tangential directions of Mars ensue (the same holds for the moon). The change in the potential field of a planet of radius r , subjected to a perturbation in potential Φ due to an orbiting moon, is denoted by ϕ and can be expressed as a spherical harmonics expansion in time domain as (in what follows we rely on the formulation of Efroimsky & Makarov, 2014)

$$\phi_n(R,t) = k_n \left(\frac{R}{r}\right)^{n+1} \Phi_n(R,R^*), \tag{1}$$

where n indicates the spherical harmonic degree, k_n is the potential Love operator of degree n, R^* is the position of the perturbing body, and R is a point on Mars's surface. The displacement Love operators, h_n and l_n express the resultant vertical (radial) and horizontal (tangential) displacements at the surface of the planet as $h_n\Phi_n/g$ and $l_n\nabla\Phi_n/g$, respectively, where g is the gravitational acceleration at the surface. In addition to the Love numbers, the magnitude of the change in gravity due to the change in the potential field is of interest. This parameter, the gravimetric factor δ, is computed as δ_n=1+2h_n/n−$k_n(n$+1/$n)$ (e.g., Agnew, 2015).

In the frequency domain, equation (1) can be written as

$$\phi_n\left(R,\omega_{pq}^{nm}\right)=\left(\frac{R}{r}\right)^{n+1}\overline{k}_n\left(\omega_{pq}^{nm}\right)\overline{\Phi}_n\left(R,R^*,\omega_{pq}^{nm}\right), \tag{2}$$

where ω_{pq}^{nm} are the Fourier tidal modes, nm and pq are integers used to number the modes, and $\overline{k}_n$ is the complex frequency-dependent Love number where $\overline{k}_n(\omega_{pq}^{nm})=\Re\left[\overline{k}_n(\omega_{pq}^{nm})\right]+i\Im\left[\overline{k}_n(\omega_{pq}^{nm})\right]$. The Love number k_n can be written as $|\overline{k}_n|\exp(-i\epsilon_n)$, where ϵ_n is the phase angle between the tidal force and resulting bulge and equals the geometric lag (λ_{pq}^{nm}) (labeled "tidal lag" in Figure 1) through $\lambda_{pq}^{nm}=\epsilon_{pq}^{nm}/m$ (e.g., Efroimsky & Makarov, 2013). The phase angle is also related to the energy that is being dissipated in the tides as 1/Q_n, where Q_n is the tidal quality factor of spherical harmonic degree n

$$Q_n=\frac{1}{\sin|(\epsilon_n)|}=\frac{\sqrt{\Re^2(k_n)+\Im^2(k_n)}}{|\Im(k_n)|}. \tag{3}$$

For the terrestrial planets, ϵ_n is usually small at the main tidal periods (except when the satellite is very close to the resonance period), as a result of which Q_n can be approximated by

$$Q_n\approx\frac{1}{\tan|(\epsilon_n)|}=\frac{\Re(k_n)}{|\Im(k_n)|}. \tag{4}$$

In the following section, we turn our attention to intrinsic shear attenuation.

2.2. Viscoelastic Dissipation Models

While elasticity is a result of bond stretching along crystallographic planes in an ordered solid, viscosity and dissipation inside a polycrystalline material occur by motion of point, linear, and planar defects, facilitated by diffusion. In viscoelastic behavior, each of these mechanisms contribute (e.g., Karato, 2008). Deformations of a viscoelastic solid depend on the temporal scale of the applied load (Chawla & Meyers, 1999). For small stresses, the stress-strain relation is linear, and the response is described in the time domain via the creep function $J(t)$. The creep function links material properties and forcing (as input) with the "felt" (relaxed) shear modulus and phase lag due to attenuation (as output). The response of the material to forcing consists of an instantaneous elastic response followed by a semirecoverable transient flow regime where the strain rate changes with time and finally yields to steady state creep. Based on this, the general form of the creep function for a viscoelastic solid consists of three terms:

$$\underbrace{J(t)}_{\text{Creep function}}=\underbrace{J_U}_{\text{Elastic}}+\underbrace{f(t)}_{\text{Transient strain -rate}}+\underbrace{t/\eta}_{\text{Viscous}}, \tag{5}$$

where t is time and η is the steady state Newtonian viscosity. The relaxed shear modulus (G_R) and the associated dissipation (Q_μ^{-1}) are obtained from the following expressions:

$$G_R(\omega)=\left\{\Re(\hat{J}(\omega))^2+\Im^2[\hat{J}(\omega)]\right\}^{-\frac{1}{2}}, \tag{6}$$

$$Q_\mu^{-1}\approx|\Im[\hat{J}(\omega)]|/\Re[\hat{J}(\omega)], \tag{7}$$

where $\hat{J}(\omega)$ is the complex compliance. Note that Q_μ is an intrinsic material property and therefore different from the global Q_n discussed in the previous section (cf. equation (3)). Briefly, the distinction between global tidal dissipation (Q_n) and intrinsic attenuation (Q_μ), which is a spatially varying material property and responsible for the attenuation of, for example, seismic waves, derives from the fact that Q_n, in addition to "sensing" Q_μ, is also influenced by gravity and inertial effects due to rotation of the planet. At reasonably high frequencies, this distinction becomes redundant as Q_n approaches Q_μ (see also discussion in Efroimsky, 2015 and Lau et al., 2016).

In the following, we consider a suite of laboratory-based viscoelastic dissipation models: Maxwell, extended Burgers, Andrade, Sundberg-Cooper, and a power law scheme. These models derive from grain size-,

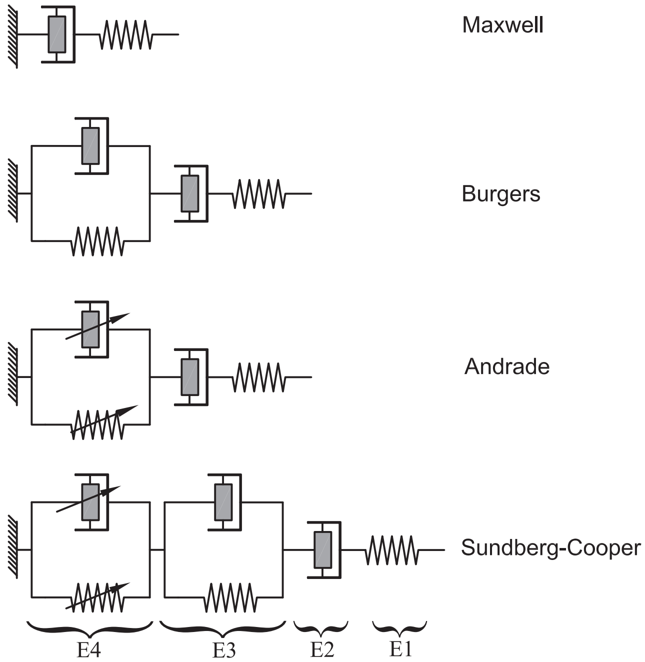

Figure 2. Schematic representation of the viscoelastic models in terms of springs and dashpots. A spring element (E1) represents a purely elastic response, whereas a dashpot element (E2) is representative of purely viscous damping. A series connection of elements 1 and 2 is representative of the response of a Maxwell model (irrecoverable), whereas a connection of elements 1 and 2 in parallel (element 3) results in an anelastic (recoverable) response with a discrete (single) spectrum of relaxation times. Arrows on spring and dashpot in element 4, conversely, indicate an element that incorporates a continuous distribution of anelastic relaxation times and results in a broadened response spectrum. Modified from Renaud and Henning (2018).

temperature-, and pressure-sensitive viscoelastic relaxation measurements. The dissipation models based on extended Burgers, Andrade, and the power law scheme are described in detail in Jackson and Faul (2010) and rely on laboratory experiments (temperature range 800–1200° C) of torsional forced oscillation data (period range 1–1,000 s) on melt-free polycrystalline olivine (grain sizes in the range 3–165 μm). The model of Sundberg and Cooper (2010) is also based on torsional oscillation data of fine-grained (5-μm) peridotite (olivine+39 vol% orthopyroxene) in the temperature range 1200–1300° C and periods of 1 to ∼200 s.

As shown in Figure 2, each model can be represented as an arrangement of springs and dashpots connected in series, in parallel, or a combination of both (Cooper, 2002; Findley & Onaran, 1965; Jackson, 2007; McCarthy & Castillo-Rogez, 2013; Moczo & Kristek, 2005; Nowick & Berry, 1972). The instantaneous elastic response is mimicked by a spring (element 1, E1) and the fully viscous behavior by that of a dashpot (element 2, E2). The series connection (i.e., a Maxwell module), includes a nonrecoverable displacement, while a parallel connection (a Voigt module) ensures fully recoverable deformations with either a discrete (element 3, E3) or a continuous distribution (element 4, E4, henceforth “modified” Voigt module) of anelastic relaxation times. These models have been applied in various circumstances to model the response of planetary bodies. In the following, we briefly describe each of these models that are employed later to model tidal dissipation within Mars.

2.2.1. Maxwell

Maxwell is the simplest model for expressing the viscoelastic behavior and is represented by a series connection of a spring and dashpot. The associated creep function of this model is

$$J(t) = \underbrace{J_U}_{1} + \underbrace{\frac{t}{\eta}}_{E2}. \tag{8}$$

Here, J_U is the unrelaxed, that is, infinite-frequency, compliance, and E1 and E2 represent spring and dashpot elements (cf. Figure 2), respectively. The compliance for this model is

$$\hat{J} = J_U - \frac{i}{\omega}, \tag{9}$$

and real and imaginary parts of the complex shear modulus, $\hat{G}=1/\hat{J}$, are computed from

$$\Re[\hat{G}(\omega)] = \frac{\tau_M{}^2\omega^2}{J_U(\tau_M{}^2\omega^2+1)}, \tag{10}$$

$$\Im[\hat{G}(\omega)] = \frac{\tau_M\omega}{J_U(\tau_M{}^2\omega^2+1)}, \tag{11}$$

where $\tau_M=\eta/G_U$ is the Maxwell time, and G_U is the unrelaxed shear modulus. As is apparent from comparison of (6) and (8), this model does not include a transient phase and immediately drops to the viscous fluid regime from the elastic response. Hence, while this model represents a reasonable approximation for very long-period loading such as glacial isostatic adjustments (Peltier, 1974), it does not suffice for modeling the viscoelastic behavior at intermediate periods. An extended form of Maxwell's model is employed in this study, where effects of grain size, temperature, and pressure are accounted for through a modification of the Maxwell time (τ_M; e.g., Jackson & Faul, 2010; McCarthy et al., 2011; Morris & Jackson, 2009) according to

$$\tau_M(T,P,d) = \tau_{M0}\left(\frac{d_g}{d_0}\right)^{m_{gv}} \exp\left[\left(\frac{E^*}{R}\right)\left(\frac{1}{T}-\frac{1}{T_0}\right)\right]\exp\left[\left(\frac{V^*}{R}\right)\left(\frac{P}{T}-\frac{P_0}{T_0}\right)\right], \tag{12}$$

where R is the gas constant, E^* is activation energy, V^* is activation volume, d_g is grain size, m_{gv} is grain size exponent for viscous relaxation, P is pressure, T is temperature, and τ_{M0} is a normalized value at a particular set of reference conditions (d_0, P_0, and T_0). Parameter values used here and in the following are tabulated in Table A1.

2.2.2. Extended Burgers

The shortcoming of Maxwell's model in representing a transient response between elastic and viscous regimes can be rectified by introducing a time-dependent anelastic transition between the two regimes. This implies connecting a Voigt module (E3) and a Maxwell module (E1 and E2 connected in series) as shown in Figure 2. For this model, the creep function takes the form

$$J(t) = \underbrace{J_U}_{\text{E1}} + \underbrace{\Delta J\left[1-\exp\left(-\frac{t}{\tau}\right)\right]}_{\text{E3}} + \underbrace{\frac{t}{\eta}}_{\text{E2}}, \tag{13}$$

where E3 corresponds to the anelastic time-dependent response, J_U is, as before, unrelaxed compliance, respectively, ΔJ is the magnitude of the anelastic contribution, and τ is the time constant for the development of the anelastic response. More generally, the single anelastic relaxation time τ can be replaced by a distribution $D(\tau)$ of relaxation times over an interval specified by upper (τ_H) and lower bounds (τ_L; Jackson & Faul, 2010). From a micromechanical point of view, this distribution is associated with diffusionally accommodated grain boundary sliding for which dissipation varies monotonically with temperature and period. The creep function of the material takes the form

$$J(t) = J_U\left[1 + \Delta\int_{\tau_L}^{\tau_H} D(\tau)\left[1-\exp\left(-\frac{t}{\tau}\right)\right]\mathrm{d}\tau + \frac{t}{\tau_M}\right], \tag{14}$$

where Δ is the fractional increase in compliance associated with complete anelastic relaxation and is called the anelastic relaxation strength. A commonly used distribution of anelastic relaxation times associated with the monotonic background dissipation is the absorption band model proposed by Minster and Anderson (1981)

$$D_B(\tau) = \frac{\alpha\tau^{\alpha-1}}{{\tau_H}^{\alpha}-{\tau_L}^{\alpha}}, \qquad 0<\alpha<1, \tag{15}$$

for $\tau_L<\tau<\tau_H$ and 0 elsewhere. Jackson and Faul (2010) found that their experimental data were better fit by including a dissipation peak in the distribution of anelastic relaxation times, which is superimposed upon the monotonic background along with the associated dispersion. This background peak is mostly attributed to sliding with elastic accommodation of grain boundary incompatibilities (see Takei et al., 2014, for a different view). The distribution for such a peak is given by

$$D_P(\tau) = \frac{1}{\sigma\tau\sqrt{2\pi}}\exp\left(\frac{-\ln\left(\frac{\tau}{\tau_P}\right)}{2\sigma^2}\right). \tag{16}$$

With this, the components of the dynamic compliance become

$$\Re[\hat{J}(\omega)] = J_U\left(1 + \Delta\int_{\tau_L}^{\tau_H}\frac{D(\tau)}{1+\omega^2\tau^2}\mathrm{d}\tau\right), \tag{17}$$

$$\Im[\hat{J}(\omega)] = J_U\left(\omega\Delta\int_{\tau_L}^{\tau_H}\frac{\tau D(\tau)}{1+\omega^2\tau^2}\mathrm{d}\tau + \frac{1}{\omega\tau_M}\right). \tag{18}$$

Note that τ_L and τ_H define the cutoffs of the absorption band, where dissipation is frequency-dependent ($\propto\omega^{\alpha}$). The lower bound of the absorption band ensures a finite shear modulus at high frequencies and restricts attenuation at these periods.

All involved timescales (τ_M, τ_L, τ_H, and τ_P) are considered to be grain size, pressure, and temperature dependent through (Jackson & Faul, 2010)

$$\tau_i(T,P,d) = \tau_{i0}\left(\frac{d_g}{d_0}\right)^{m_g}\exp\left[\left(\frac{E^*}{R}\right)\left(\frac{1}{T}-\frac{1}{T_0}\right)\right]\exp\left[\left(\frac{V^*}{R}\right)\left(\frac{P}{T}-\frac{P_0}{T_0}\right)\right], \tag{19}$$

where all parameters are as before (cf. equation (12)) and i=M,L,H,P. The grain size exponent m_g can be different in the case of anelastic (m_{ga} for i=L,H,P) and viscous relaxation (m_{gv} for i=M), respectively. To more realistically account for variations of the unrelaxed shear modulus with temperature and pressure, Jackson and Faul (2010) suggest the following modification

$$J_U(T,P) = \left[G_U(T_0,P_0) + (T-T_0)\frac{\partial G_U}{\partial T} + (P-P_0)\frac{\partial G_U}{\partial P}\right]^{-1}. \quad (20)$$

Values for the temperature and pressure derivatives are given in Table A1.

2.2.3. Andrade

Whereas the extended Burgers model incorporates a distribution of relaxation times within a restricted timescale to account for transient anelasic relaxation, Andrade's model proposes a distribution of relaxation times in the entire time domain (represented by arrows on spring and dashpot). The resultant configuration of a Maxwell module and a modified Voigt module (E4) is illustrated in Figure 2, which results in a creep function of the form (Andrade, 1962)

$$J(t) = \underbrace{J_U}_{\text{E1}} + \underbrace{\beta t^\alpha}_{\text{E4}} + \underbrace{\frac{t}{\eta}}_{\text{E2}}, \quad (21)$$

where β qualitatively has the same role as Δ in the extended Burgers model, and α represents the frequency dependence of the compliance. In this model, the absorption band extends from 0 to ∞. This implies that anelastic relaxation effectively contributes across the entire frequency range from short-period seismic waves to geological timescales. Consequently, Andrade's model is more economically parameterized than the extended Burgers model. Real and imaginary parts of the dynamic compliance are

$$\mathfrak{R}[\hat{J}(\omega)] = J_U\left[1 + \beta^* \Gamma(1+\alpha)\omega^{-\alpha}\cos\left(\frac{\alpha\pi}{2}\right)\right], \quad (22)$$

$$\mathfrak{I}[\hat{J}(\omega)] = J_U\left[\beta^* \Gamma(1+\alpha)\omega^{-\alpha}\sin\left(\frac{\alpha\pi}{2}\right) + \frac{1}{\omega\tau_M}\right], \quad (23)$$

where β^*=β/J_U and Γ is the Gamma function. Note that Andrade's model incorporates a broader absorption band (theoretically of infinite width) compared to the extended Burgers model, which ultimately results in frequency-dependent dissipation at all timescales. Following Jackson and Faul (2010), corrections due to grain size, temperature, and pressure are applied through a pseudoperiod master variable, X, which replaces the actual period

$$X = \omega^{-1}\left(\frac{d_g}{d_0}\right)^{-m_g}\exp\left[\left(\frac{-E^*}{R}\right)\left(\frac{1}{T} - \frac{1}{T_0}\right)\right]\exp\left[\left(\frac{-V^*}{R}\right)\left(\frac{P}{T} - \frac{P_0}{T_0}\right)\right]. \quad (24)$$

2.2.4. Sundberg-Cooper

To model dissipation for the combined effects of diffusional background and elastically accommodated grain boundary sliding, Sundberg and Cooper (2010) introduced a composite creep function. Their model represents a modification to Andrade's model in order to improve its functionality over a broader frequency range and to account for the variation of the "felt" elastic response as it has to match the unrelaxed compliance (J_U) at high frequencies and the relaxed compliance (J_R) at low frequencies. This model graphically consists of two Voigt modules and a Maxwell module (cf. Figure 2); one module is similar to that used in Andrade's model (E4), whereas the other module is equivalent to that of the extended Burgers model (E3). The creep function for the Sundberg-Cooper model is thus

$$J(t) = \underbrace{J_U}_{\text{E1}} + \underbrace{\delta J\left[1 - \exp\left(-\frac{t}{\tau}\right)\right]}_{\text{E3}} + \underbrace{\beta t^\alpha}_{\text{E4}} + \underbrace{\frac{t}{\eta}}_{\text{E2}}, \quad (25)$$

where all variables are as before. Similar to what has been implemented for the extended Burgers model, the corresponding term (E3 in equation (25)), can be replaced by an integral specifying a distribution of anelastic relaxation times τ as prescribed by equation (14), and modifications for grain size, temperature, and pressure are allowed for through equation (19). Also, accounting for the influence of these parameters in the modified Voigt module (E4 in equation (25)) is implemented in a similar fashion to Andrade's model through the pseudoperiod master variable X (equation (24)). With this in mind, the real and imaginary parts of the dynamic compliance for the Sundberg-Cooper model are

$$\mathfrak{R}[\hat{J}(\omega)] = J_U\left[1+\beta^{*}\Gamma(1+\alpha)\omega^{-\alpha}\cos\left(\frac{\alpha\pi}{2}\right)+\Delta\int_{\tau_L}^{\tau_H}\frac{D(\tau)}{1+\omega^2\tau^2}\mathrm{d}\tau\right], \tag{26}$$

$$\mathfrak{I}[\hat{J}(\omega)] = J_U\left[\beta^{*}\Gamma(1+\alpha)\omega^{-\alpha}\sin\left(\frac{\alpha\pi}{2}\right)+\omega\Delta\int_{\tau_L}^{\tau_H}\frac{\tau D(\tau)}{1+\omega^2\tau^2}\mathrm{d}\tau+\frac{1}{\omega\tau_M}\right]. \tag{27}$$

2.2.5. Power Law Approximation

As a final model, we consider a power law approximation, which was originally proposed as a means of fitting earlier measurements (Jackson et al., 2002). This model is not based on physical principles but merely represents an approximation of shear dissipation. The power law scheme requires that $Q_\mu^{-1} \ll 1$. Similar to the Andrade and Sundberg-Cooper models, this model also employs a pseudoperiod master variable to account for the effects of temperature, pressure, and grain size, defined similar to X in equation (24) with $m_g = 1$ (Jackson & Faul, 2010). The power law for Q_μ takes the form

$$Q_\mu^{-1} = AX^{\alpha}, \tag{28}$$

where A is the power law coefficient. The shear modulus dispersion associated with this model is

$$\frac{G(\omega)}{G_U} = 1 - \cot\left(\frac{\alpha\pi}{2}\right)Q_\mu^{-1}(\omega). \tag{29}$$

2.3. Comparing the Sensitivity of the Rheological Models

Before applying the aforementioned dissipation models to Mars, it is informative to consider the sensitivity of intrinsic material properties to a number of key variables. Here, we focus on the dispersion of shear modulus G_R and attenuation factor Q_μ with forcing period, temperature, and grain size (all at constant pressure), which is shown in Figure 3. All parameter values used to compute the response curves are compiled in Table A1. First off, we notice that both G_R and Q_μ vary considerably within the range of forcing periods considered here, which includes the tidal forcing periods of the Sun and Phobos and those of long- and short-period seismic waves (vertical lines in Figures 3a and 3b). Most of the short-period seismic band (periods <1 hr) is governed by a broad, low-relaxation strength, high-frequency plateau (arrow in Figure 3b), characteristic of elastically accommodated grain boundary sliding (E3 in Figure 2), which for tidal periods (>1 hr) gives way to a continuous distribution of anelastic relaxation times, characteristic of the high-temperature background (E4 in Figure 2). It has to be noted though that the exact location (in time) of the various processes is currently not well resolved.

In general, the same features are observed in the plots showing temperature variations (Figures 3c and 3d) throughout most of the ranges of interest for tidal studies. In the range of high Q_μ, that is, at short periods, low temperatures, and large grain sizes, the behavior of the extended Burgers and Sundberg-Cooper models is due to the existence of a background dissipation peak (less apparent) associated with elastically accommodated grain boundary sliding (E3), which occurs around 1300–1400 K, although the interpretation of the background peak is less clear and is currently unexplained by any existing model (Gribb & Cooper, 1998; Raj & Ashby, 1975; Takei et al., 2014). Based on the relative variation of the response curves, we would expect to see little difference between the Andrade, extended Burgers, and Sundberg-Cooper models. Due to the relaxed shear modulus behavior, Andrade and the extended Burgers models are similar as expected based on Figure 2, while the response of the Sundberg-Cooper model is expected to be slightly different in the seismic band.

Relative to forcing period and temperature, Q_μ appears to vary little with grain size (Figure 3e), whereas G_R undergoes significant changes for very small grain sizes (<0.1 mm; Figure 3f). In contrast, the largest changes in Q_μ occur in the range of relatively large grain sizes (10–100 mm). Because of the relative flatness of the extended Burgers and Sundberg-Cooper models in the aforementioned range, compared to both Andrade and power law, the latter two are more likely to resolve (large) grain sizes. Also, since small grain sizes are accompanied by a considerable reduction in G_R, which is equivalent to an overall "softening," and, as a consequence, a potentially significant change in tidal response, small grain sizes are less likely to accord with observations. Incidentally, the grain size insensitivity of the extended Burgers model, in addition to preferential sampling of relative large grain sizes, was observed in the previous work by Khan et al. (2018).

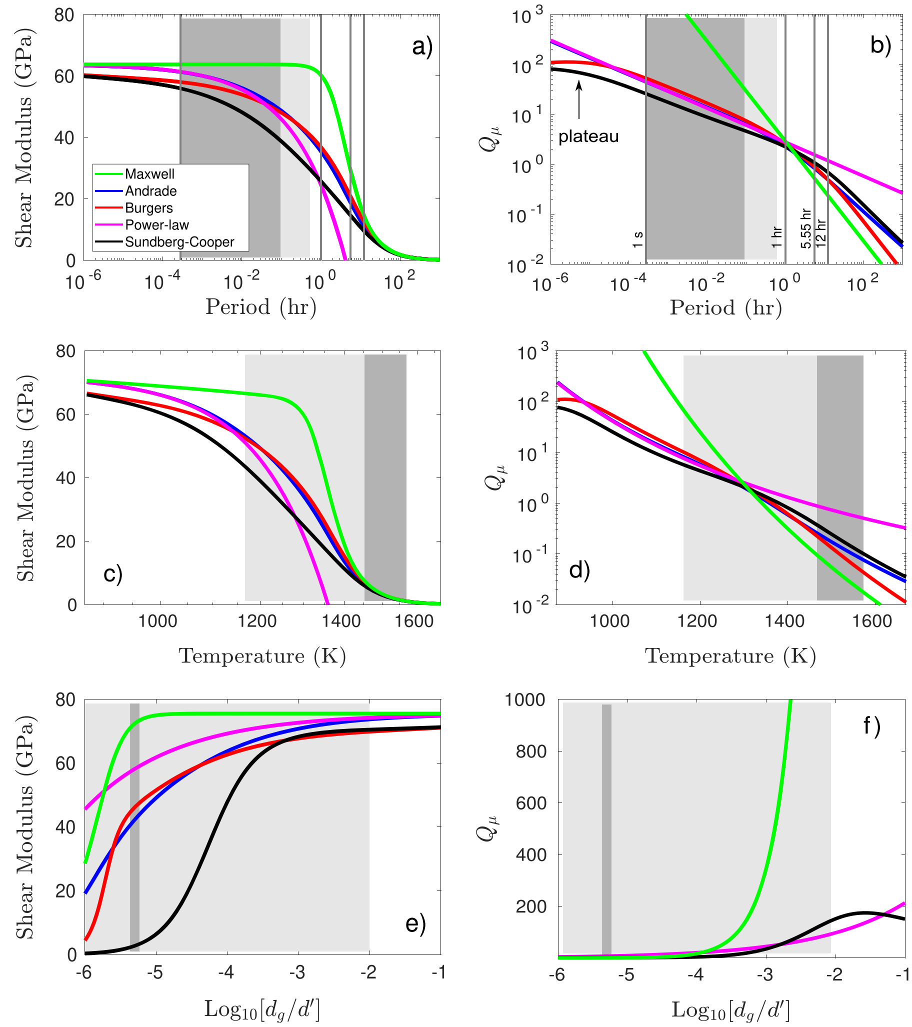

Figure 3. Computed variations of relaxed shear modulus (G_R) and shear attenuation (Q_μ) with period, temperature, and grain size for the five rheological models considered in this study. (a, b) G_R and Q_μ as a function of period at constant temperature and grain size; the vertical lines show periods of interest: seismic body waves (1 s), normal modes (1 hr), main tidal excitation of Phobos (5.55 hr), and main tidal excitation of the Sun (12.32 hr). (c, d) G_R and Q_μ as a function of temperature at constant period and grain size. (e, f) G_R and Q_μ as a function of grain size at constant period and temperature. Light and dark shaded areas denote the ranges covered by the experimental measurements of Jackson and Faul (2010) and Sundberg and Cooper (2010), respectively. All curves were produced at a constant pressure of 10.4 GPa and for an unrelaxed shear modulus of 65 GPa. Viscoelastic parameter values employed are given in Table A1, and d'=1 m.

It is readily recognized from this comparison that the behavior of Maxwell's model is distinct. In fact, the aforementioned lack of a transient response from elastic to viscous behavior is clearly visible in Figure 3 as a sudden drop-off in G_R. While the Maxwell model clearly shows evidence of frequency-dependent dissipation, the latter is too strong to be representative of dissipation in planetary materials. As indicated in Figure 3, the tidal periods of Mars lie in the intermediate range, where a composite of both elastic and viscous regimes contribute to the response—a feature that is incompatible with Maxwell's model. This will be discussed further in section 5.2.4. As for the power law, the other simplified rheological model, it shows behavior that appears compatible with the three main models in the restricted range of low temperatures, seismic periods (~1 s to 30 min), and larger grain sizes. However, since this model, like Andrade, lacks a cutoff in the frequency-dependent absorption band, both show similar behavior in the aforementioned parameter range.

As a preliminary summary, we can make the following predictions: (1) The response of Maxwell's model is such that it is unlikely to match geophysical observations throughout most of the period range of interest; (2) the long-period and high-temperature behavior of the power law scheme is not realistic; (3) the Andrade,

Table 1
Martian Geophysical Data, Uncertainties, and Sources

Quantity	Symbol	Value and uncertainty	Reference
Mean density	$\bar{\rho}$	3,935 ± 1.2 kg/m^3	Rivoldini et al. (2011)
Mean moment of inertia	I/MR^2	0.36379 ± 0.0001	Konopliv et al. (2016)
Tidal Love number	k_2	0.169 ± 0.006	Konopliv et al. (2016)
Global quality factor	Q_2	95 ± 10	Khan et al. (2018)
Mass	M	$6.417{\cdot}10^{23}{\pm}2.981{\cdot}10^{19}$ kg	Konopliv et al. (2016)
Radius	R	3,389.5 km	Seidelmann et al. (2002)

Note. Tidal Love number and global quality factor are referenced to the main tidal period of Phobos (5.55 hr).

extended Burgers, and Sundberg-Cooper models provide qualitatively similar responses over most of the period and temperature range considered here, although Andrade, as expected, is less dissipative at the very longest periods and highest temperatures. The similarity of the three models is not surprising given that they contain many of the same elements as shown in Figure 2. These observation will be quantitatively assessed in the following, where the laboratory-based dissipation models are combined with geophysical inverse modeling.

3. Geophysical Data

In this study we focus on mean density ($\bar{\rho}$), normalized mean moment of inertia (I/MR^2), and tidal response in the form of the second-degree tidal Love number (k_2) and global tidal dissipation or tidal quality factor (Q_2). The data are discussed in detail in the literature (e.g., Genova et al., 2016; Khan et al., 2018; Lainey et al., 2007; Konopliv et al., 2016; Nimmo & Faul, 2013; Rivoldini et al., 2011; Yoder et al., 2003) and need not be repeated here. The geophysical data are summarized in Table 1.

4. Computational Aspects

Formally, predicting data (**d**) from a set of model parameters (**m**) is usually written as **d**=g(**m**), where g embodies the physical laws that connect **m** and **d**. In the present case, g comprises a set of algorithms (g_1,...,g_4) as a result of which **d**=g(**m**) can be written as

$$\underbrace{\text{Model parameters}}_{\text{section 4.1}} \xrightarrow{g_1} \underbrace{\text{Mineralogy}}_{\text{section4.2}} \xrightarrow{g_2} \underbrace{\text{Elastic properties}}_{\text{section4.2}} \xrightarrow{g_3} \underbrace{\text{Viscoelasticity}}_{\text{section2.2}} \xrightarrow{g_4} \underbrace{\text{Data}}_{\text{table 1}}$$

In the following, we describe the steps needed to compute "synthetic" data ($\bar{\rho}$, I/MR^2, k_2, and Q_2) from the model parameters.

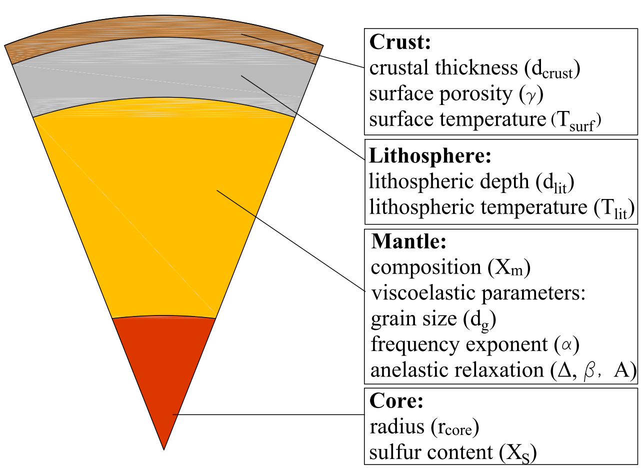

Figure 4. Schematic diagram illustrating model parameterization. The model is spherically symmetric and divided into crust, lithosphere, mantle, and core. These four layers are parameterized using the parameters shown in the boxes on the right. For more details see main text (section 4.1).

4.1. Model Parameterization and Prior Model Distribution

We assume a spherically symmetric model of Mars consisting of crust, lithosphere, mantle, and core as illustrated in Figure 4.

Crust and Mantle. In line with the previous work (Khan & Connolly, 2008; Khan et al., 2018), crust and mantle compositions are parameterized in terms of major element composition in the model chemical system CFMASNa (comprising the oxides of the elements CaO-FeO-MgO-Al_2O_3-SiO_2-Na_2O), a system that accounts for more than 98% of the mass of Mars' silicate envelope. Crust and mantle compositions are fixed in this study and are compiled in Table 3. The crust is further parameterized in terms of thickness and surface porosity. Porosity γ is assumed to vary linearly from the surface to the bottom of the Moho (of thickness d_{crust}), where porosity vanishes due to pressure. The lithosphere is described by thickness (d_{lit}) and temperature (T_{lit}). Within the crust and lithosphere, temperature is computed by a linear areothermal gradient that is determined from a fixed surface temperature ($T_{surface}$) and lithospheric temperature and depth. The

Table 2
Viscoelastic Model Parameters and Prior Distributions

Viscoelastic model	Parameters and prior information				
	α	d_g (mm)	β	Δ_B	A
Distribution	Uniform	Log-uniform	Log-uniform	Uniform	Uniform
Andrade	0.2–0.6	0.001–50	10^{-14}–10^{-9}	—	—
Extended Burgers	0.2–0.6	0.001–50	—	0.9–2	—
Power law	0.2–0.6	0.001–50	—	—	0.001–0.01
Sundberg-Cooper	0.2–0.6	0.001–50	10^{-14}-10^{-9}	0.9–2	—

sublithospheric mantle adiabat is defined by the entropy of the lithology at the temperature T_{lit} and at depth d_{lit}, which also defines the location where the conductive lithospheric geotherm intersects the mantle adiabat.

Mantle Viscoelasticity. Parameters needed to compute mantle viscoelasticity depend on the chosen rheological model (section 2.2). The two important parameters that are common to all of the rheological models are grain size (d_g) and frequency dependence (α). In addition to these two parameters, we consider anelastic relaxation strengths Δ_B and β and power law model coefficient A as variable parameters given their importance in determining viscoelastic behavior. Activation energy (E^*) and volume (V^*) were shown to be of less relevance in the previous work by Khan et al. (2018). All other viscoelastically related parameters are fixed and given in Table A1.

Core. As in most geophysical models of Mars, we assume that S is the dominant light element (1) because Si, C, and O are not sufficiently soluble in an Fe-rich liquid at the low pressures that are expected to have been maintained during core formation (Stevenson, 2001) and (2) due to the observed depletion of chalcophile elements, notably S, of the Martian meteorities (McSween & McLennan, 2014). Following previous work (e.g., Khan et al., 2018; Rivoldini et al., 2011), the core is assumed to be liquid, convecting, and well mixed and parameterized in terms of radius (r_{core}), sulfur content (X_S), and temperature (adiabat). The core adiabat is not independent of the mantle adiabat but determined so that the thermodynamically computed temperature at the core-mantle boundary provides the input temperature for the core adiabat.

Finally, all parameters and prior model parameter distributions are summarized in Tables 2–4.

4.2. Computing Elastic and Viscoelastic Properties

To compute stable mantle mineralogy, seismic wave velocities, and density along self-consistent mantle adiabats as functions of pressure and composition in the CFMASNa model chemical system, we follow previous work (e.g., Khan & Connolly, 2008; Khan et al., 2018) and employ Gibbs free energy minimization (Connolly, 2009). For this purpose, the thermodynamic formulation of Stixrude and Lithgow-Bertelloni (2005b) and parameters of Stixrude and Lithgow-Bertelloni (2011) are used. Pressure is obtained by integrating the surface load. In the context of computing mantle properties, we would like to note that the pressure and temperature derivatives of the shear modulus (equation (20)) employed earlier (section 2.3) are not used here as these are determined as part of the free energy minimization. To account for the effect of porosity on crustal seismic P and S wave velocities (V_P and V_S) and density (ρ), all three parameters are multiplied by the depth-dependent porosity.

To compute elastic properties of the core in the FeS system, we rely on the parameterization of Rivoldini et al. (2011). Since the core is assumed to be fluid, it does not support shear and consequently no shear dissipation occurs. Hence, its response only includes the buoyant component and it is completely in quadrature with the acting force. In line with previous work, bulk dissipation is considered negligible. Finally, to “convert” the elastic (unrelaxed) shear moduli to viscoelastic (relaxed) moduli, we compute shear attenuation (Q_μ) and relaxed shear moduli using the equations described in section 2.2 for each of the rheological models. Shear attenuation in the crust and lithosphere is fixed to Q_{lit}=1,000. As for the core, we assume that dissipation only occurs in shear. This seems appropriate given that dissipation in bulk is negligible (Benjamin et al., 2006).

10.1029/2019JE006015

Table 3
Major Element Crust and Mantle Compositions Used in This Study

Component	Crust	Mantle
CaO	7.0	2.4
FeO	18.8	18.7
MgO	9.2	30.7
Al_2O_3	10.9	3.5
SiO_2	50.7	44.1
Na_2O	3.3	0.6

Note. Crust and mantle compositions are from Taylor and McLennan (2008) and Taylor (2013). All numbers in weight percent.

4.3. Computing Tidal Response

To determine the frequency-dependent tidal response of a spherically symmetric, self-gravitating, and viscoelastic planetary model, we use an adaptation of the method and code developed by Al-Attar and Tromp (2014) and Crawford et al. (2018) for modeling glacial loading. This approach is based on the generalized spherical harmonic expansions (Phinney & Burridge 1973) of the displacement field and gravitational potential perturbation and leads to a complete decoupling between the radial expansion coefficients for each spherical harmonic degree and order. The resulting ordinary differential equations are then efficiently solved using a one-dimensional spectral element discretization. Inertial terms in the equations of motion are neglected within these calculations due to the tidal periods being well below those of the gravest free oscillations. Quasi-static deformation in the fluid core is modeled following the approach of Dahlen (1974), with the inclusion of tidal forces requiring a slight modification of the theory as described in Appendix B. The resulting code calculates the Love numbers k_n, h_n, and l_n along with the quality factors Q_n for any spherical harmonic degree. Mean density and mean moment of inertia are readily obtained from integration of the density profile.

4.4. Inverse Problem

The inverse problem **d**=g(**m**) is solved using a Bayesian approach (e.g., Mosegaard & Tarantola, 1995)

$$\sigma(\mathbf{m}) = \varkappa f(\mathbf{m})\mathscr{L}(\mathbf{m}), \tag{30}$$

where $\varkappa$ is a normalization constant, $f(\mathbf{m})$ is the prior model parameter distribution, $\mathscr{L}(\mathbf{m})$ is the likelihood function, and $\sigma(\mathbf{m})$ is the posterior model parameter distribution and represents the solution to the inverse problem. The form of $\mathscr{L}(\mathbf{m})$ is determined from data, their uncertainties, and data noise (to be described below). To sample the posterior distribution, we employ the Metropolis algorithm, which is an importance sampling algorithm. This stochastic algorithm, which is based on a Markov chain Monte Carlo method, ensures that models that fit data (through $\mathscr{L}(\mathbf{m})$) and are consistent with the chosen prior model parameter distribution (through $f(\mathbf{m})$) are sampled preferentially.

As concerns the likelihood function, we assume that data noise is Gaussian distributed and that observational uncertainties and modeling errors among the different data sets are independent. As a consequence, the likelihood function takes the form

$$\mathscr{L}(\mathbf{m}) \propto \prod_{\mathrm{i}} \exp\left(-\frac{|\mathrm{d}^{\mathrm{i}}_{\mathrm{obs}} - \mathrm{d}^{\mathrm{i}}_{\mathrm{cal}}(\mathbf{m})|^2}{2\sigma_{\mathrm{i}}^2}\right), \tag{31}$$

where the integer i is either $\overline{\rho}$, I/MR^2, k_2, or Q_2, and $\mathrm{d}_{\mathrm{obs}}$ and $\mathrm{d}_{\mathrm{cal}}(\mathbf{m})$ refer to observed and calculated synthetic data, respectively, and σ is the uncertainty associated with each data set. For each rheological model, we

Table 4
Crust, Lithosphere, Mantle, and Core Model Parameters and Prior Distributions

Parameter	Description	Interval	Distribution
γ	Surface porosity	0.5–0.65	Uniform
d_{crust}	Crustal thickness	10–90 km	Uniform
Q_{lit}	Shear attenuation in crust and lithosphere	1,000	Fixed
T_{surface}	Surface temperature	0 °C	Fixed
d_{lit}	Lithospheric depth	100–400 km	Uniform
T_{lit}	Lithospheric temperature	700–1450 °C	Uniform
r_{core}	Core radius	0–3,000 km	Uniform
X_S	Core sulfur content	0–100%	Uniform

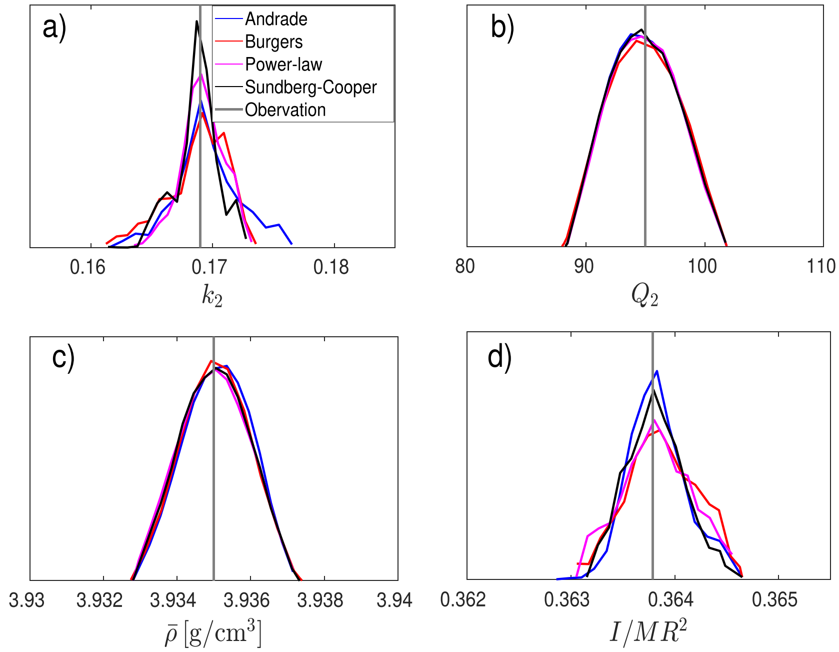

Figure 5. Computed data distributions showing fit to observations for each of the rheological models: (a) second-degree tidal Love number k_2; (b) second-degree global tidal dissipation Q_2; (c) mean density $\bar{\rho}$; and (d) mean moment of inertia I/MR^2. The results shown in (a) and (b) refer to the main tidal period of Phobos. The vertical solid lines indicate observed values of k_2, Q_2, $\bar{\rho}$, and I/MR^2. Observations and uncertainties are compiled in Table 1.

sampled around 100,000 models in total and to ensure near-independence, every twentieth model was retained for analysis. This number is obtained from analyzing the autocorrelation of the likelihood function, which provides a measure of when independence between models has been achieved.

5. Results and Discussion

5.1. Data Fit

Here and in the following, the main focus will be on the extended Burgers, Andrade, and Sundberg-Cooper rheological models and the power law approximation scheme whereas Maxwell's model will be discussed separately in section 5.2.4. We make this distinction here based on the observation that although Maxwell's model is capable of fitting the observations (not shown), this is only achievable for unrealistically low mean viscosities. The resultant data fits are shown in Figure 5 and indicate that all four rheological models are capable of fitting the observations within uncertainties.

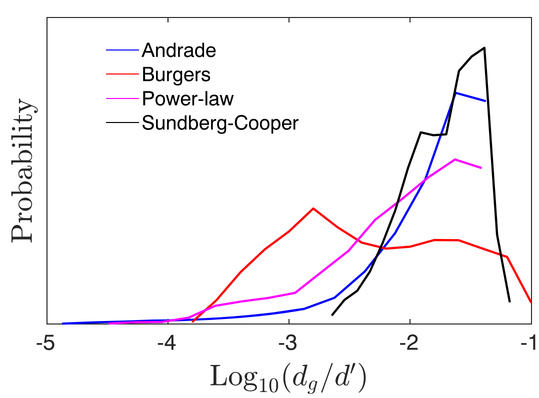

Figure 6. Sampled distributions of grain size for each viscoelastic model obtained from the inversions.

5.2. Viscoelastic Properties

5.2.1. Grain Size

Sampled grain size distributions for each of the rheological models is shown in Figure 6 and indicate that the Andrade, Sundberg-Cooper, and power law models imply larger grain sizes in comparison to those based on the extended Burgers model. The three former models suggest most probable grain sizes in the range 0.5–4 cm range, whereas in the case of the latter model, grain sizes are less well resolved with a slight preference for the range 0.1–1 cm. Importantly, the form of the sampled grain size distributions follows the behavior observed in Figure 3 closely: Andrade, Sundberg-Cooper, and power law show the largest variation in the range ~1–10 cm, while the extended Burgers model is relatively "flat" in the 0.1–10 cm range, in agreement with the earlier work (Khan et al., 2018).

Table 5
Summary of Inversion Results for the Viscoelastic Model Parameters Considered in This Study

Parameter	Andrade	Extended Burgers	Power law	Sundberg-Cooper
d_g	0.1–2 cm	0.01–4 cm	0.1–2 cm	1–4 cm
α	0.22–0.38	0.22–0.42	0.22–0.38	0.24–0.38
$-\log_{10}(\beta)$	12.4–13	—	—	13.5–14
Δ_B	—	1–1.5	—	1.1–1.4
A	—	—	0.0015–0.0025	—

Note. Quoted ranges cover the 90% credible interval.

In general, grain sizes obtained in this study are larger than observed in terrestrial samples, where grains of submillimeter-to-millimeter size are typically found (Karato, 1984). Incidentally, relatively large grain sizes (~1–10 cm) are also found in a study by Lau and Faul (2019), where the extended Burgers model was applied to Earth's deep mantle to model its anelastic response (see also section 5.2.2).

In support of larger grain sizes, it is shown in previous work (Khan et al., 2018) how the geophysical results could be employed in tandem with geodynamic simulations to identify plausible geodynamic scenarios and parameters. The geodynamical models were generally able to reproduce the geophysically determined areotherms, crustal thickness values, and grain sizes, but only in part, lithospheric thicknesses. Grain sizes greater than 1 mm were mainly restricted to cases of relatively strong grain growth, which tended to increase internal temperature and thicken the lithosphere beyond the current geophysical observations.

For brevity, inversion results for the other viscoelastic model parameters considered here, including frequency exponent (α), anelastic relaxation strengths (Δ_B and β), and power law coefficient (A), are summarized in Table 5.

5.2.2. Temperature and Attenuation

Inverted areothermal and shear attenuation (Q_μ) profiles are shown in Figure 7 for the major rheological models considered in this study. From this figure, we can make a number of observations. First, the obtained thermal profiles are well constrained and overlap across the entire depth range. This confirms earlier investigations (Khan et al., 2018; Nimmo & Faul, 2013) where it was shown that global tidal dissipation provides strong constraints on thermal structure. Moreover, the temperature profiles are in good agreement with the results for the extended Burgers model of Khan et al. (2018). Thus, the obtained temperature profiles are to first order independent of rheology. Second, the shear attenuation profiles overlap in the upper mantle (depth range 200–1000 km), which appears to be highly attenuating with Q_μ<100, but differ in the lower part of the mantle (depth range 1000–1600 km), where Q_μ appears to be less constrained for the Andrade and extended Burgers models. Note that although the shear attenuation profiles shown in Figure 7 are computed at the main tidal period of Phobos (5.55 hr), shear attenuation at seismic periods (1 s) are not significantly different with Q_μ remaining below 100 for most of the upper part of the mantle (not shown). This suggests that it will be difficult to distinguish between the various rheological models based on the structure of the attenuation profiles.

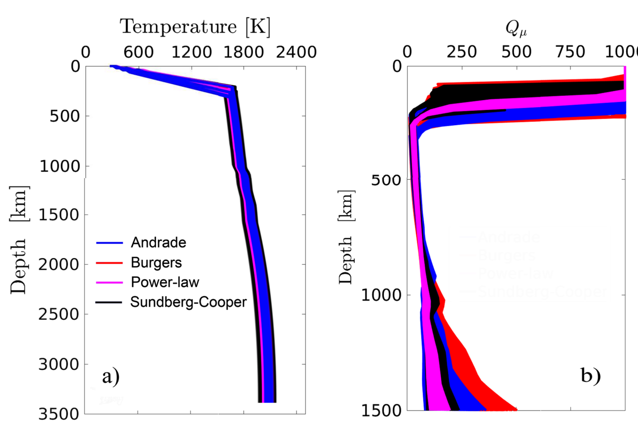

Figure 7. Inverted areothermal (a) and shear attenuation (b) profiles for the main viscoelastic models considered in this study (at the main tidal period of Phobos). Shear attenuation models are only shown down to the core-mantle boundary since the core is fluid (Q_μ=0).

From the point of view of seismology, the implications of this for the propagation and observation of, for example, seismic body and surface waves is such that their detection could be significantly impaired over regional and teleseismic distances. The detection of seismic events by the InSight seismometer (Lognonné, 2019) would therefore present a first-order test of the experimentally constrained viscoelastic models considered here in the sense that seismic waves that have spent a significant part of their traverse in the mantle from source to station are expected to be attenuated.

5.2.3. Predicted Short- and Long-Period Planetary Response

What the previous discussion suggests is that from knowledge of dissipation at a single frequency (here the main tidal period of Phobos), it appears to be difficult to distinguish between rheological models. If, however, we know the tidal response at other frequencies, more precise arguments can be made about both interior dissipative properties and corresponding rheological models as illustrated in Figure 8. Figure 8 shows the predicted probability distributions for k_2 and Q_2 at three different periods: short- (1-s) and long-period (1-hr) seismic waves, and at the main Solar tide on Mars (12.32 hr) computed for all the inverted models. First off, relative differences in computed k_2 distributions for the three different periods for a particular rheological model are minor and cover a similar range ~0.16–0.18 across all the models. In the case of Q_2, however, the distinction within and between models is significantly more pronounced. Although all four rheological models match the only existing observation of Q_2 at 5.55 hr (Figure 5), they differ in their prediction for Q_2 at the other periods. We observe similar behavior for the Andrade and power law models, on the one hand, and the extended Burgers and Sundberg-Cooper models, on the other hand. This "pairing" clearly reflects the common underlying mechanisms that exists between the models. For example, higher dissipation (lower Q_2) at higher frequencies observed for the former two models (Figures 8c, 8d, 8g, and 8h) is attributed to the presence of the extra dissipation peak, which tends to flatten the Q_μ curves and, as a result, prevents a dramatic increase of attenuation at short timescales. In contrast, since the frequency-dependent absorption band extends throughout the entire spectrum in the case of Andrade and the power law scheme, low attenuation (high Q_2) at high frequencies ensues (Figures 8a, 8b, 8e, and 8f). Note that, although intrinsic attenuation (Q_μ) plays a key role in determining the tidal quality factor (Q_2), they are not the same. As emphasized, the discrepancy is due to the role of the restoring force of gravity, which increases in importance with increasing forcing period, but is less relevant in the case of seismic waves. Clearly, observations of dissipation at other periods hold the potential of strongly constraining anelastic structure.

This is further quantified in Figure 9, which shows the degree 2 global response of Mars in the form of k_2, Q_2, and δ_2 over a much larger period range (~1 s to 10 years) for a single inverted model (maximum likelihood model for each rheology). The Q_2 response behavior (Figure 9b) for the Andrade and power law models appears to be dominated by the absorption band with a negative period dependence, which, in the case of Andrade, slowly transitions into viscous dissipation for periods >1 month up until a peak value is reached (not shown) after which friction occurs purely viscously (see also discussion in Efroimsky, 2012a). As expected, the power law scheme fails to propose realistic values of Q_2 at long periods (Figure 9b), which indicates that the Chandler wobble analysis by Zharkov and Gudkova (2009) (with a period of ~200 days) that relies on this particular rheological model probably needs to be reassessed.

In comparison, the response of the extended Burgers and Sundberg-Cooper models is more complex with a broad plateau extending from the seismic to the tidal range that merges into the absorption band with negative frequency dependence (note that the slopes determined by α, the frequency exponent, between the red and black lines are different because the inverted values for α differ for the two models). On the smaller-period side of the plateau, dissipation varies with a positive frequency dependence, whereas toward the long-period end of the response curves (>2 years), purely viscous dissipation predominates. For the particular models shown here, Phobos' tide falls in the absorption band in the case of the extended Burgers model but appears within the transition between plateau and the absorption band in the Sundberg-Cooper model. It has to be emphasized though that the relative location of the various features that dominate dissipation at different timescales (see section 2.1) are not well constrained from the observation at a single period. In summary, this figure serves to indicate that the predicted response behavior is such that from comparison of a single measurement by InSight of Q_2 above or below and/or k_2 below the main tidal period of Phobos, further constraints on interior structure and dissipative properties can be obtained.

This has been discussed in terrestrial and lunar studies, where data at different periods are available (e.g., Benjamin et al., 2006; Efroimsky, 2012a; Karato, 2013; Lau & Faul, 2019; Nimmo et al., 2012; Williams & Boggs, 2015). For example, Lau and Faul (2019) considered seismic normal mode and short- and long-period tidal dissipation measurements for the Earth in an attempt to reconcile the anelastic response of the deep mantle across timescales from ~500 s to 18.6 years. As briefly indicated earlier, the authors use the extended Burgers model and vary a number of parameters related hereto (e.g.,

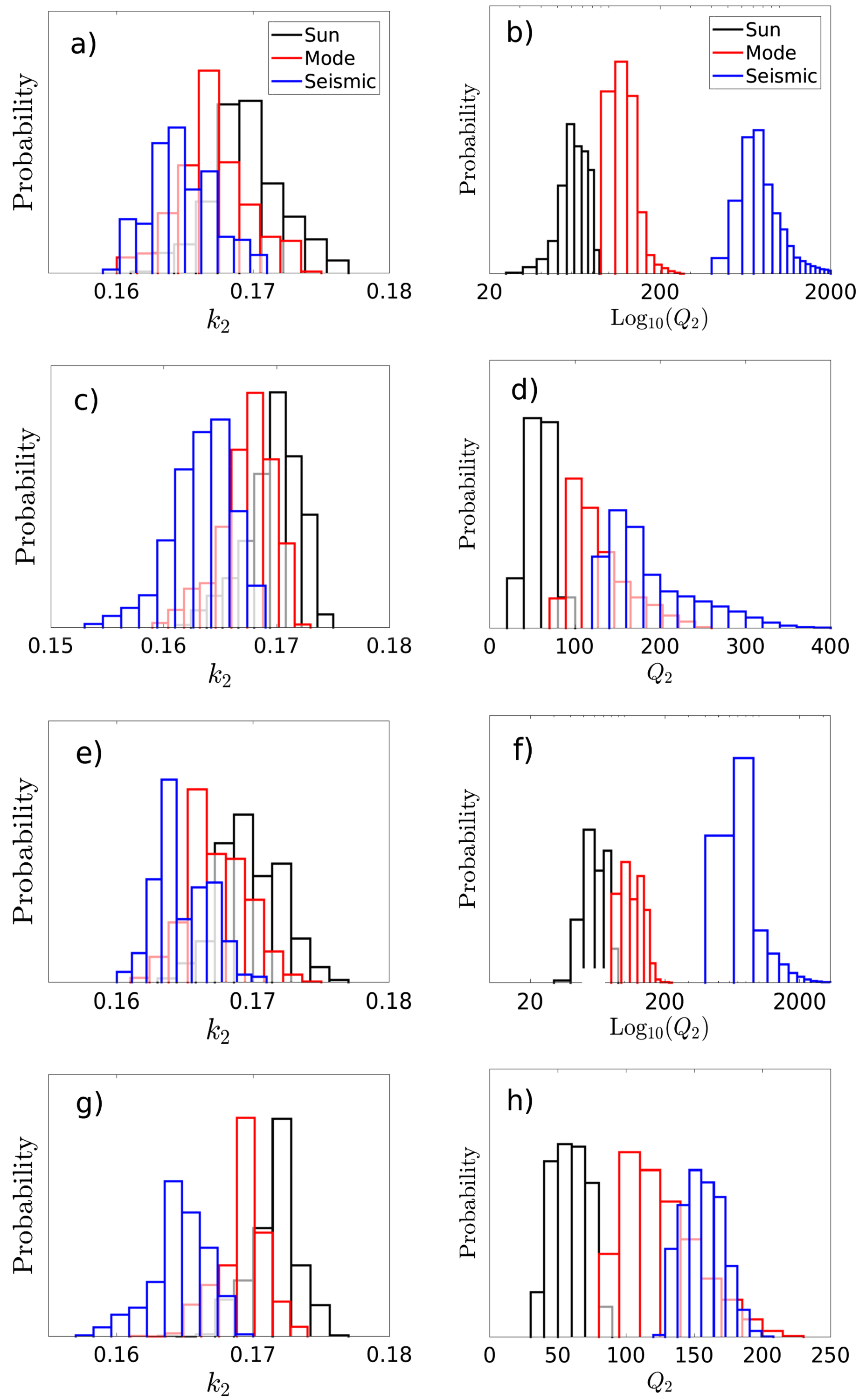

Figure 8. Sampled distributions of second-degree tidal Love number k_2 and quality factor Q_2 at three different periods of geophysical interest for each rheological model: (a, b) Andrade, (c, d) extended Burgers, (e, f) power law, and (g, h) Sundberg-Cooper. Note that because of the large variation in Q_2 for the Andrade and power law models, plots (b) and (f) are shown in terms of $\mathrm{Log}_{10}(Q_2)$. The distributions represent predictions based on the observed 5.55-hr main Phobos tide. The periods considered are 12.32 hr (solar tide), 1 hr (long-period normal modes), and 1 s (short-period body waves).

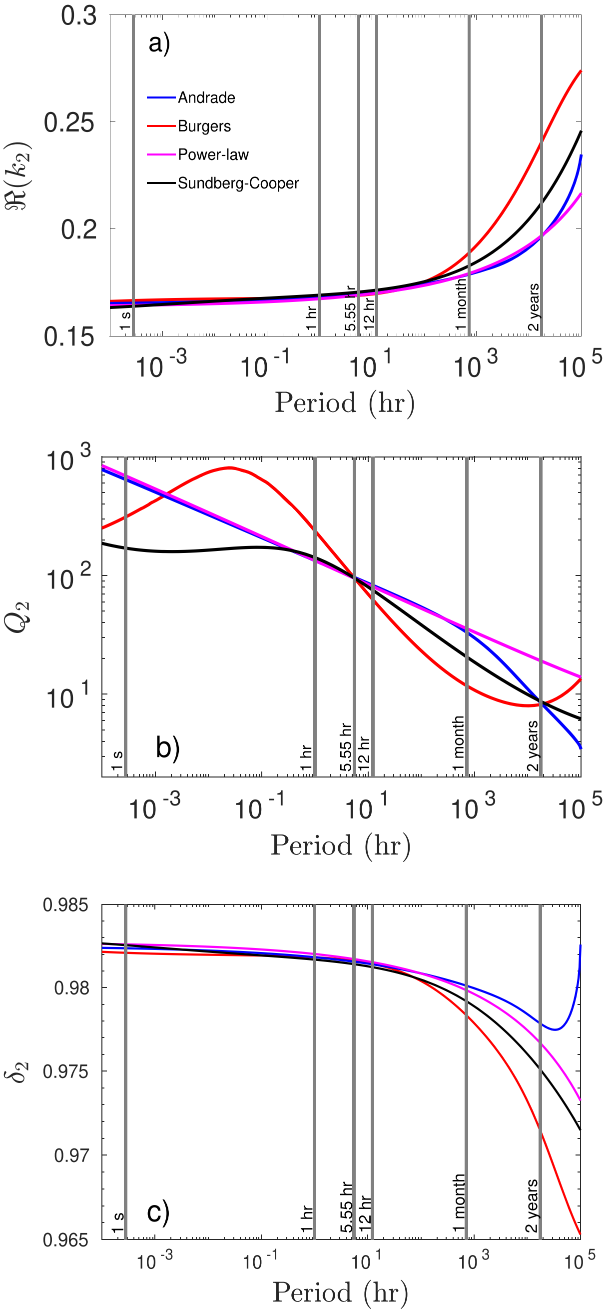

Figure 9. Computed tidal response of Mars as a function of period from short-period seismic (1 s) to long-period tidal timescales (∼10 years) for the four major rheological models considered in this study. (a) Amplitude of tidal response (real part of second-degree potential Love number k_2), (b) second-degree global tidal quality factor (Q_2), and (c) gravimetric factor (δ_2). The response curves were computed using the maximum likelihood model obtained in the inversion and the viscoelastic parameters compiled in Table A1 for each rheology.

grain size, anelastic relaxation strengths, activation energy and volume, and mantle potential temperature). The authors find that two different frequency dependencies are needed to fit normal mode and tide data. Qualitatively, the authors observe the same anelastic behavior discussed in relation to the extended Burgers model investigated here (red line in Figure 9), including the presence of a plateau that determines dissipation for periods below ∼12 hr and an absorption band above, extending to ∼20 years without clear indication of onset of viscous dissipation. As is the case for our models, the exact occurrence of the various characteristics (e.g., plateau, transition to absorption band, and α) is not well constrained.

Finally, we have computed responses at four periods (1 s, 1 hr, 5.55 hr, and 12.32 hr) for all Love numbers (k_n, h_n, and l_n), gravimetric factors δ_n, and quality factors Q_n, for the maximum likelihood models of each rheology and for n=2–5. The results are compiled in Table 6. The absolute value of Q_n is observed to decrease, that is, dissipation increases, as n becomes larger. This reflects an increased sensitivity to shallower structure, which implies that more of the dissipative part of the planet (mantle) is "seen" with increased spherical harmonic degree. The values obtained here are in good agreement with model predictions made elsewhere (e.g., Van Hoolst et al., 2003; Zharkov & Gudkova, 1997, 2005, 2009). Based on the observed variation in predicted model values (Figure 9), the phase lags Q_n are likely to be much better at discriminating between different models than are the gravimetric factors δ_n. This finding will be tested in the near future by dissipation measurements provided by both RISE and SEIS. Although beyond the scope of this study, knowledge of higher-degree harmonics are important for modeling the orbital evolution and future demise of Phobos (Black & Mittal, 2015; Burns, 1978; Efroimsky & Lainey, 2007; Rosenblatt et al., 2016).

5.2.4. Maxwell's Model

While Maxwell's model, in spite of its simplicity, is capable of fitting data within uncertainties (not shown in Figure 5) for interior structure models that match the results of the other models (see Table 7), this is only possible for very low average viscosities (∼$2{\cdot}10^{16}$ Pa·s) that are well below what is expected for the viscosity of the upper mantle of the Earth (10^{19}–10^{22} Pa·s; e.g., Cathles, 2015; Forte & Mitrovica, 2001; Peltier, 1974; Soldati et al., 2009) and therefore probably unrealistic.

Low Martian mantle viscosities have also been obtained in previous studies (Bills et al., 2005; Castillo-Rogez & Banerdt, 2012), where Maxwell's model was applied to estimate its tidal response. For a homogeneous solid model of Mars, Bills et al. (2005) and Castillo-Rogez and Banerdt (2012) found average viscosities of ∼10^{15} and ∼10^{16} Pa·s, respectively. Bills et al. (2005) argued that the presence of a liquid core could provide a possible explanation for the low viscosity, but the modeling results based on Maxwell presented here invalidate this inasmuch as a model including a fully liquid core still results in a low average viscosity. We attribute the unrealistically low viscosity values obtained from Maxwell's model to its shortcoming, particularly lack of an intermediate-stage anelastic transient response as also argued elsewhere (e.g., Castillo-Rogez et al., 2011).

10.1029/2019JE006015

Table 6
Predicted Tidal Properties of Mars Until Spherical Harmonic Degree 5 Based on the Inversion Results (Mean Values) for Individual Rheological Models at Four Different Periods: Seismic, 1 s; Mode, 1 hr; Phobos, 5.55 hr; and Solar, 12.32 hr

	Andrade				Burgers				Power law				Sundberg-Cooper			
	Seismic	Mode	Phobos	Solar	Seismic	Mode	Phobos	Solar	Seismic	Mode	Phobos	Solar	Seismic	Mode	Phobos	Solar
k_3	0.0505	0.051	0.051	0.052	0.0505	0.0518	0.052	0.0522	0.051	0.051	0.052	0.0525	0.051	0.0522	0.053	0.0529
k_4	0.0227	0.0232	0.0235	0.024	0.0233	0.0239	0.024	0.0244	0.023	0.0235	0.0237	0.024	0.0232	0.024	0.0242	0.0245
k_5	0.0134	0.0137	0.0138	0.014	0.0138	0.0142	0.0145	0.0145	0.0135	0.0138	0.0141	0.0143	0.0137	0.0143	0.0144	0.0146
h_2	0.229	0.232	0.233	0.233	0.232	0.234	0.235	0.235	0.23	0.232	0.233	0.233	0.23	0.237	0.238	0.238
h_3	0.103	0.105	0.105	0.105	0.105	0.106	0.106	0.106	0.103	0.105	0.105	0.105	0.104	0.107	0.108	0.108
h_4	0.061	0.063	0.063	0.063	0.062	0.064	0.064	0.064	0.061	0.063	0.063	0.063	0.062	0.065	0.065	0.065
h_5	0.045	0.046	0.046	0.046	0.046	0.048	0.048	0.048	0.045	0.046	0.046	0.046	0.046	0.048	0.048	0.048
δ_2	0.9845	0.98	0.9795	0.978	0.9845	0.9805	0.98	0.98	0.984	0.98	0.978	0.978	0.9855	0.98275	0.983	0.98
δ_3	1.001	1.002	1.002	1.001	1.003	1.002	1.001	1.001	1.001	1.002	1.001	1.000	1.001	1.002	1.001	1.001
δ_4	1.002	1.003	1.002	1.002	1.002	1.002	1.002	1.002	1.002	1.002	1.002	1.002	1.002	1.003	1.002	1.002
δ_5	1.006	1.006	1.006	1.006	1.006	1.006	1.006	1.006	1.006	1.006	1.005	1.005	1.006	1.006	1.006	1.006
l_2	0.037	0.038	0.038	0.038	0.038	0.04	0.04	0.04	0.037	0.039	0.039	0.039	0.038	0.04	0.04	0.04
l_3	0.0064	0.0066	0.0066	0.0066	0.0065	0.007	0.0073	0.0073	0.0064	0.0066	0.0067	0.0067	0.0067	0.0071	0.0073	0.0073
l_4	0.003	0.003	0.003	0.003	0.003	0.003	0.003	0.003	0.003	0.003	0.003	0.003	0.0032	0.0032	0.0032	0.0032
l_5	0.0018	0.0019	0.0019	0.0019	0.0019	0.002	0.002	0.002	0.00185	0.002	0.002	0.002	0.00198	0.0021	0.0021	0.0021
Q_3	700	152	83	75	185	152	82	75	800	142	83	77	172	157	82	75
Q_4	700	137	70	66	170	150	66	65	700	130	70	67	158	140	68	65
Q_5	650	115	65	58	155	115	57	52	650	108	60	55	150	130	58	53

Note. Harminic degrees n=3, 4, and 5 correspond to forcing periods of 3.7, 2.775, and 2.22 hrs, respectively.

Table 7
Summary of Inversion Results for Each of the Rheological Models Considered in This Study

Parameter	Unit	Andrade	Extended Burgers	Power law	Sundberg-Cooper	Maxwell
Crustal thickness (T_{crust})	km	50–75	50–75	50–70	50–75	45–60
Lithospheric depth (d_{lit})	km	225–350	225–340	225–300	225–325	180–350
Lithospheric temperature (T_{lit})	K	1,650–1,670	1,650–1,690	1,640–1,670	1,630–1,690	1,560–1,585
CMB temperature	K	1,830–1,940	1,860–1,910	1,830–1,910	1,780–1,950	1,930–1,990
Core radius (r_{core})	km	1,790–1,850	1,750–1,810	1,790–1,850	1,760–1,840	1,830–1,890
Core sulfur content (X_S)	wt%	18–19.5	17–19	18–19	17–19	19.5–20.5
Viscosity (η)	Pa·s	—	—	—	—	$2 \cdot 10^{16}$

Note. Ranges indicate the 90% credible interval. CMB refers to the core-mantle boundary.

In an attempt to overcome the lack of an appropriate transient regime, alternative models, including Burgers and Andrade, have been considered (Sohl & Spohn, 1997; Castillo-Rogez & Banerdt, 2012). Relying on a Burgers model with a single relaxation time (cf. equation (13)), Sohl and Spohn (1997) obtained effective mantle viscosities in the range 10^{13}–10^{15} Pa·s that are similar to those of Bills et al. (2005), and therefore imply inadequate treatment of the transient regime in such a model. Considering an Andrade rheology, Castillo-Rogez and Banerdt (2012), on the other hand, obtained more "realistic" mantle viscosities of 10^{19}–10^{22} Pa·s, indicating improved treatment of the anelastic transient process.

5.3. Interior Structure

Since this study focuses on modeling and understanding the anelastic response of Mars at tidal and seismic frequencies, we briefly summarize the results on interior structure. Inverted model parameters are presented in Table 7 and profiles of P and S wave speed and density are shown in Figure 10. Since both inverted model parameter values seismic profiles largely overlap, the results can not be used to distinguish between the viscoelastic models with the exception of Maxwell. Not surprisingly, the results are in good agreement with those of Khan et al., 2018, where the influence of compositional parameters was considered in detail in the context of an extended Burgers viscoelastic model. Here as there, models imply relatively large cores (∼1,750–1,850 km in radius) with a significant complement of S (∼17–20 wt%). As the core S content found here is close to the eutectic composition and core-mantle boundary temperatures and pressures are in excess of 1800 K and ∼19–20 GPa, respectively, a solid inner core is unlikely to be present (e.g., Helffrich, 2017; Stewart et al., 2007). Moreover, a large core implies that the counterpart of a terrestrial bridgmanite-dominated lower mantle in Mars is unlikely to be present with potentially important implications for the dynamic evolution of Mars's mantle (e.g., Breuer et al., 1997; Ruedas et al., 2013; van Thienen et al., 2006). For further discussion of interior structure, we refer the reader to previous work (e.g., Khan et al., 2018; Nimmo & Faul, 2013; Plesa et al., 2016; Rivoldini et al., 2011; Smrekar et al., 2019).

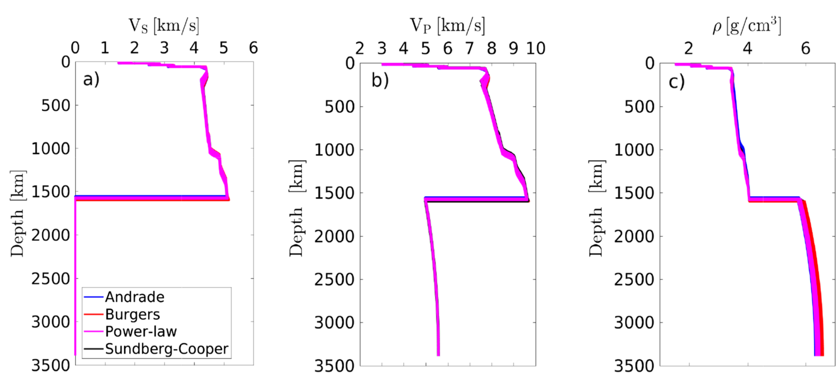

Figure 10. Inverted seismic wave speed and density profiles obtained for each of the rheological models. (a) P wave speed (V_P), (b) S wave speed (V_S), and (c) density (ρ).

6. Discussion and Conclusion

In this study, we have examined the geophysical implications of a series of grain size-, temperature-, and frequency-dependent laboratory-based viscoelastic models. These models have been developed in an attempt to describe dissipative properties of planetary materials on the macroscopic scale in terms of interactions that occur on the microscopic scale, that is, on the level of atoms and grains. The rheological models are based on deformation experiments of melt-free polycrystalline olivine and an olivine-pyroxene mixture, respectively, and include Maxwell, Andrade, extended Burgers, Sundberg-Cooper, and a power law scheme.

We combined the viscoelastic models with phase equilibrium computations to allow for self-consistently constructed models of seismic elastic and anelastic properties and tested the resultant models against global geophysical observations for Mars. All of the models were found to be able to match the Martian observations including tidal response (amplitude and phase) and mean mass and moment of inertia. The simplest of the investigated rheological models, that of Maxwell, whose response only consists of a purely elastic and a viscous component, only matched the observations for very low viscosities ($\sim 10^{16}$ Pa·s). This observation is in accord with previous work, where similar results were obtained. Based on the observation that the main tidal periods of most solar system objects are to be found in the transient period range where Maxwell is singularly deficient, it appears reasonable to conclude that Maxwell's model should be abandoned in favor of more realistic models such as Andrade, extended Burgers, or Sundberg-Cooper. These models represent improvements relative to Maxwell inasmuch as these models include an anelastic transient regime that allows for generating significant dissipation in the main tidal period range.

Of the other models investigated, all converged upon the same results in terms of interior structure parameters, that is, the results are to first order insensitive of the exact nature of the attenuation mechanisms that account for dissipation of energy in planetary interiors. While we only examined a single frequency associated with the main tide of Phobos, our results show that from knowledge of the response at an additional period, significantly improved constraints on interior properties can be derived. InSight observations of tidal phase lags will prove particularly rewarding since these appear to be a much better means of discriminating between different models than either tidal amplitudes or induced surface displacements.

As shown here, application of our method yields a host of quantitative predictions and results. In particular, the method also provides insights into future requirements of, for example, improvements in experimental data, that will be needed for modeling more complex models. Chief among these are (more discussion is given in Nimmo & Faul, 2013, and Khan et al., 2018) the following: (a) extending the forced torsional oscillation experiments to minerals beyond olivine, including compositions that are more Fe-rich and therefore more representative of Martian mantle compositions; (b) extending the experimental conditions to longer periods; (c) consideration of the effects of hydration and partial melt, which can significantly impact viscosity by lowering it and thereby increase dissipation (Cline et al., 2018; Jackson et al., 2004; Karato, 2013; Takei, 2017); and (d) including grain size variation with depth in view of geodynamic models that show evidence for grain growth with depth (e.g., Rozel, 2012), which would tend to lower dissipation, requiring increased dissipation elsewhere.

For community use, we computed and tabulated predicted model responses (Love numbers and attenuation) at a number of distinct periods and spherical harmonic degree for each of the rheological models considered here. Since the amount of energy that is being dissipated in planetary interiors depends on rheology, the latter effectively controls the orbital evolution of binaries such as Mars and Phobos and therefore provides an improved means for, for example, understanding the future demise of Phobos.

Ultimately, it is the expectation that InSight, which has been operative on the surface of Mars since the end of November 2018, will enable separate measurements of k_2, Q_2, and δ_2 (and maybe k_3 and δ_3). More specifically, and in addition to the direct measurement of the tidal response by RISE, different schemes have been proposed to employ the SEIS instrument to extract the tidal response from the seismic data, by having the very broad-band seismometer act as a gravimeter to measure Mars's response to tidal forces (Pou et al., 2018).

As a final remark, we would like to note that although we have focused on Mars, the methodology developed here is generally formulated and therefore applicable to other solar and extrasolar system bodies, where tidal

Table A1
Compilation of Viscoelastic Parameters Used in This Study

Parameter	Value	Unit	Viscoelastic model
β	$3.2{\cdot}10^{-13}$	$Pa^{-1}\ s^{-0.33}$	A
β	$0.5{\cdot}10^{-13}$	$Pa^{-1}\ s^{-0.33}$	SC
Δ_B	1.4	—	ExtB, SC
α	0.33	—	All
A	0.002	$s^{-0.33}$	PL
d_0	13.4	μm	All
P_0	0.2	GPa	All
T_0	1,173	K	All
τ_{L0}	10^{-3}	s	ExtB, SC
τ_{H0}	10^{7}	s	ExtB, SC
τ_{M0}	$10^{7.48}$	s	All
τ_{P0}	$10^{-3.4}$	s	ExtB, SC
Δ_P	0.057	—	ExtB, SC
m_{ga}	1.3	—	A, M, ExtB, SC
m_{gv}	3	—	A, M, ExtB, SC
V^*	10^{-5}	m^3/mol	All
E^*	360	kJ/mol	All
$\partial G/\partial P$	1.8	—	All
$\partial G/\partial T$	−13.6	MPa/K	All
σ	4	—	ExtB, SC

Note. The values of $\partial G/\partial P$ and $\partial G/\partial T$ are only employed for creating the models discussed in section 2.3. All parameter values used are from Jackson and Faul (2010), except for β and A (SC and PL), which are based on forward model runs such that the modeled Q_μ and G_R (shown in Figure 3) among the various rheologies have comparable amplitudes. A = Andrade; ExtB = extended Burgers; M = Maxwell; PL = power law; SC = Sundberg-Cooper.

constraints are available to determine interior structure and properties. In particular, we envision applying our method to the Moon for which tidal dissipation measurements at several periods are available.

Appendix A: Viscoelastic Parameters

Table A1 compiles the viscoelastic parameter values used throughout this study.

Appendix B: Further Details About Tidal Calculations

To model tidal deformation within the planet, we make use of the quasi-static momentum equation (e.g., Al-Attar & Tromp, 2014; Dahlen, 1974; Tromp & Mitrovica, 1999)

$$-\nabla\cdot\mathbf{T} + \nabla(\rho\mathbf{u}\cdot\nabla\Phi) - \nabla\cdot(\rho\mathbf{u})\nabla\Phi + \rho\nabla(\phi+\psi) = \mathbf{0}, \tag{B1}$$

where $\mathbf{T}$ denotes the incremental Lagrangian-Cauchy stress tensor, ρ the equilibrium density, $\mathbf{u}$ the displacement vector, Φ the equilibrium gravitational potential, ϕ the perturbed gravitational potential, and ψ is the tidal potential that we have now added into the problem. The sign conventions used in this section follow those in Al-Attar and Tromp (2014). The tidal potential is assumed to have an exponential time dependence at a given forcing frequency. Due to the linearity of the equations of motion, the displacement and gravitational potential have the time dependence, and the common exponential factors have been canceled from all equations. The frequency dependence within the problem then arises solely from the fact that the appropriate viscoelastic modulii are evaluated at the prescribed tidal frequency.

As shown by Dahlen (1974), for static or quasi-static problems this linearized Lagrangian description is only valid within solid parts of the Earth model. Within the fluid core, the displacement vector is not well defined, and Dahlen (1974) instead showed that all relevant fields can be expressed in terms of the perturbed gravitational potential ϕ. In particular, we can write the first-order perturbations to density ρ' and pressure p' in the fluid core as

$$p' = -\rho(\phi+\psi), \quad \rho' = g^{-1}\partial_r\rho(\phi+\psi), \tag{B2}$$

where $g{=}\partial_r\Phi$. These identities generalize those presented in Dahlen (1974) to include the applied tidal potential, but their derivation is essentially unchanged. The gravitational potential perturbation itself is then a solution of the following modified Poisson equation

$$(4\pi G)^{-1}\Delta^2\phi = \begin{cases} -\nabla\cdot(\rho\mathbf{u}) & \text{in solid regions} \\ g^{-1}\partial_r\rho(\phi+\psi) & \text{in fluid regions} \\ 0 & \text{outside the planet} \end{cases} \tag{B3}$$

where G is Newton's gravitational constant. The boundary and continuity conditions for the problem can be found in detail in Al-Attar and Tromp (2014). Within the tidal problem, however, there is no applied surface load, while the tidal potential ψ appears within the continuity conditions on the linearized traction across fluid-solid boundaries via its occurrence in the pressure perturbation p' in fluid regions.

For numerical work, it is most convenient to express the problem in its weak form. The derivation follows closely that given in Al-Attar and Tromp (2014), requiring only slight changes due to the inclusion of the tidal potential in the momentum equation, the modified Possion equation, and in the traction boundary conditions at fluid-solid boundaries. The final result is given by

$$\mathscr{A}(\mathbf{u},\phi|\mathbf{u}',\phi') \quad +\int_{M_S}\rho\nabla\psi\cdot\mathbf{u}'\,\mathrm{d}V+\int_{M_F}g^{-1}\partial_r\rho\psi\phi'\,\mathrm{d}V$$
$$+\int_{\sum_{FS}}\rho^{-}\psi\mathbf{u}'\cdot\hat{\mathbf{n}}\,\mathrm{d}S-\int_{\sum_{SF}}\rho^{+}\psi\mathbf{u}'\cdot\hat{\mathbf{n}}\,\mathrm{d}S=0, \tag{B4}$$

where $\mathscr{A}$ is the bilinear form defined in equation (2.52) of Al-Attar and Tromp (2014); ($\mathbf{u}'$,ϕ') are test functions for the displacement and potential, respectively; M_S denotes the solid regions of the model; M_F the fluid regions; Σ_{FS} and Σ_{SF} denote the fluid-solid boundaries, where the first subscript indicates whether the region on the inside of the boundary is solid (S) or fluid (F); and finally ρ^- and ρ^+ denote, respectively the equilibrium density evaluated on the lower or upper sides of a boundary. As the tidal potential only modifies the force term for the problem, the numerical implementation was readily made within the loading code developed by Al-Attar and Tromp (2014), which has been subsequently refined and improved by Crawford et al. (2018).

Acknowledgments
We are grateful to two anynomous reviewers for comments that improved the manuscript. We would also like to thank Michael Efroimsky and Francis Nimmo for additional suggestions. This work was supported by a grant from the Swiss National Science Foundation (SNF Project 172508 "Mapping the internal structure of Mars"). This is InSight contribution number 92. The interior structure models computed here, including inverted model parameters, are available online (at https://doi.org/10.5281/zenodo.3364726).

References

A, G., Wahr, J., & Zhong, S. (2014). The effects of laterally varying icy shell structure on the tidal response of Ganymede and Europa. *Journal of Geophysical Research: Planets*, *119*, 659–678. https://doi.org/10.1002/2013JE004570

Abers, G. A., Fischer, K., Hirth, G., Wiens, D., Plank, T., Holtzman, B. K., et al. (2014). Reconciling mantle attenuation-temperature relationships from seismology, petrology, and laboratory measurements. *Geochemistry, Geophysics, Geosystems*, *15*, 3521–3542. https://doi.org/10.1002/2014GC005444

Agnew, D. (2015). *Earth tides. Treatise on geophysics and geodesy*. New York: Elsevier.

Al-Attar, D., & Tromp, J. (2014). Sensitivity kernels for viscoelastic loading based on adjoint methods. *Geophysical Journal International*, *196*(1), 34–77. https://doi.org/10.1093/gji/ggt395

Andrade, E. (1962). The validity of the t1/3 law of flow of metals. *Philosophical Magazine*, *7*(84), 2003–2014.

Bellis, C., & Holtzman, B. (2014). Sensitivity of seismic measurements to frequency-dependent attenuation and upper mantle structure: An initial approach. *Journal of Geophysical Research: Solid Earth*, *119*, 5497–5517. https://doi.org/10.1002/2013JB010831

Benjamin, D., Wahr, J., Ray, R. D., Egbert, G. D., & Desai, S. D. (2006). Constraints on mantle anelasticity from geodetic observations, and implications for the J_2 anomaly. *Geophysical Journal International*, *165*, 3–16. https://doi.org/10.1111/j.1365-246X.2006.02915.x

Bierson, C. J., & Nimmo, F. (2016). A test for Io's magma ocean: Modeling tidal dissipation with a partially molten mantle. *Journal of Geophysical Research: Planets*, *121*, 2211–2224. https://doi.org/10.1002/2016JE005005. ,

Bills, B. G., Neumann, G. A., Smith, D. E., & Zuber, M. T. (2005). Improved estimate of tidal dissipation within Mars from MOLA observations of the shadow of Phobos. *Journal of Geophysical Research*, *110*, E07004. https://doi.org/10.1029/2004JE002376

Black, B. A., & Mittal, T. (2015). The demise of Phobos and development of a Martian ring system. *Nature Geoscience*, *8*(12), 913–917.

Breuer, D., Yuen, D. A., & Spohn, T. (1997). Phase transitions in the Martian mantle: Implications for partially layered convection. *Earth and Planetary Science Letters*, *148*, 457–469. https://doi.org/10.1016/S0012-821X(97)00049-6

Burns, J. A. (1978). The dynamical evolution and origin of the Martian moons. *Vistas in Astronomy*, *22*, 193–210.

Castillo-Rogez, J. C., & Banerdt, W. B. (2012). Impact of anelasticity on Mars' dissipative properties—Application to the InSight mission, *The mantle of Mars: Insights from theory, geophysics, high-pressure studies, and meteorites, LPI Contributions* (Vol. 1684, pp. 4).

Castillo-Rogez, J. C., Efroimsky, M., & Lainey, V. (2011). The tidal history of Iapetus: Spin dynamics in the light of a refined dissipation model. *Journal of Geophysical Research*, *116*, E09008. https://doi.org/10.1029/2010JE003664

Cathles, L. M. (2015). *Viscosity of the Earth's mantle* (Vol. 1362). Princeton: Princeton University Press.

Chawla, K. K., & Meyers, M. (1999). *Mechanical behavior of materials*. Upper Saddle River: Prentice Hall.

Choblet, G., Tobie, G., Sotin, C., Běhounková, M., Čadek, O., Postberg, F., & Souček, O. (2017). Powering prolonged hydrothermal activity inside Enceladus. *Nature Astronomy*, *1*(12), 841.

Cline, C. II, Faul, U., David, E., Berry, A., & Jackson, I. (2018). Redox-influenced seismic properties of upper-mantle olivine. *Nature*, *555*(7696), 355.

Connolly, J. A. D. (2009). The geodynamic equation of state: What and how. *Geochemistry, Geophysics, Geosystems*, *10*, Q10014. https://doi.org/10.1029/2009GC002540

Cooper, R. F. (2002). Seismic wave attenuation: Energy dissipation in viscoelastic crystalline solids. *Reviews in Mineralogy and Geochemistry*, *51*(1), 253–290.

Correia, A. C., Boué, G., Laskar, J., & Rodríguez, A. (2014). Deformation and tidal evolution of close-in planets and satellites using a Maxwell viscoelastic rheology. *Astronomy & Astrophysics*, *571*, A50.

Crawford, O., Al-Attar, D., Tromp, J., Mitrovica, J. X., Austermann, J., & Lau, H. C. P. (2018). Quantifying the sensitivity of post-glacial sea level change to laterally varying viscosity. *Geophysical Journal International*, *214*(2), 1324–1363. https://doi.org/10.1093/gji/ggy184

Dahlen, F. A. (1974). On the static deformation of an Earth model with a fluid core. *Geophysical Journal*, *36*, 461–485. https://doi.org/10.1111/j.1365-246X.1974.tb03649.x

Dumoulin, C., Tobie, G., Verhoeven, O., Rosenblatt, P., & Rambaux, N. (2017). Tidal constraints on the interior of Venus. *Journal of Geophysical Research: Planets*, *122*, 1338–1352. https://doi.org/10.1002/2016JE005249

Efroimsky, M. (2012a). Tidal dissipation compared to seismic dissipation: In small bodies, earths, and super-earths. *The Astrophysical Journal*, *746*, 150. https://doi.org/10.1088/0004-637X/746/2/150

Efroimsky, M. (2012b). Bodily tides near spin-orbit resonances. *Celestial Mechanics and Dynamical Astronomy*, *112*(3), 283–330. https://doi.org/10.1007/s10569-011-9397-4

Efroimsky, M. (2015). Tidal evolution of asteroidal binaries. Ruled by viscosity. Ignorant of rigidity. *The Astronomical Journal*, *150*(4), 98.

Efroimsky, M., & Lainey, V. (2007). Physics of bodily tides in terrestrial planets and the appropriate scales of dynamical evolution. *Journal of Geophysical Research*, *112*, E12003. https://doi.org/10.1029/2007JE002908

Efroimsky, M., & Makarov, V. V. (2013). Tidal friction and tidal lagging. Applicability limitations of a popular formula for the tidal torque. *The Astrophysical Journal*, *764*, 26. https://doi.org/10.1088/0004-637X/764/1/26

Efroimsky, M., & Makarov, V. V. (2014). Tidal dissipation in a homogeneous spherical body. I. Methods. *The Astrophysical Journal*, *795*(1), 6.

Faul, U., & Jackson, I. (2015). Transient creep and strain energy dissipation: An experimental perspective. *Annual Review of Earth and Planetary Sciences*, *43*, 541–569. https://doi.org/10.1146/annurev-earth-060313-054732

Findley, L., & Onaran, K. (1965). *Creep and relaxation of nonlinear viscoelastic materials*. New York: Dover Publications.

Folkner, W. M., Dehant, V., Le Maistre, S., Yseboodt, M., Rivoldini, A., Van Hoolst, T., et al. (2018). The rotation and interior structure experiment on the InSight mission to Mars. *Space Science Reviews*, *214*(5), 100.

Forte, A. M., & Mitrovica, J. X. (2001). Deep-mantle high-viscosity flow and thermochemical structure inferred from seismic and geodynamic data. *Nature*, *410*, 1049–1056.

Genova, A., Goossens, S., Lemoine, F. G., Mazarico, E., Neumann, G. A., Smith, D. E., & Zuber, M. T. (2016). Seasonal and static gravity field of Mars from MGS, Mars Odyssey and MRO radio science. *Icarus*, *272*, 228–245. https://doi.org/10.1016/j.icarus.2016.02.050

Gribb, T. T., & Cooper, R. F. (1998). Low-frequency shear attenuation in polycrystalline olivine: Grain boundary diffusion and the physical significance of the Andrade model for viscoelastic rheology. *Journal of Geophysical Research*, *103*(B11), 27,267–27,279.

Harada, Y., Goossens, S., Matsumoto, K., Yan, J., Ping, J., Noda, H., & Haruyama, J. (2014). Strong tidal heating in an ultralow-viscosity zone at the core-mantle boundary of the Moon. *Nature Geoscience*, *7*, 569–572. https://doi.org/10.1038/ngeo2211

Hauck, S. A., Margot, J.-L., Solomon, S. C., Phillips, R. J., Johnson, C. L., Lemoine, F. G., et al. (2013). The curious case of Mercury's internal structure. *Journal of Geophysical Research: Planets*, *118*, 1204–1220. https://doi.org/10.1002/jgre.20091

Helffrich, G. (2017). Mars core structure—Concise review and anticipated insights from InSight. *Progress in Earth and Planetary Science*, *4*(1), 24. https://doi.org/10.1186/s40645-017-0139-4

Henning, W. G., O'Connell, R. J., & Sasselov, D. D. (2009). Tidally heated terrestrial exoplanets: Viscoelastic response models. *The Astrophysical Journal*, *707*(2), 1000.

Hussmann, H., & Spohn, T. (2004). Thermal-orbital evolution of Io and Europa. *Icarus*, *171*(2), 391–410. https://doi.org/10.1016/j.icarus.2004.05.020

Jackson, I. (2007). Properties of rock and minerals—Physical origins of anelasticity and attenuation in rock, *Treatise on geophysics*. Amsterdam: Elsevier.

Jackson, I., & Faul, U. H. (2010). Grainsize-sensitive viscoelastic relaxation in olivine: Towards a robust laboratory-based model for seismological application. *Physics of the Earth and Planetary Interiors*, *183*, 151–163. https://doi.org/10.1016/j.pepi.2010.09.005

Jackson, I., Faul, U. H., Gerald, J. D. F., & Tan, B. H. (2004). Shear wave attenuation and dispersion in melt-bearing olivine polycrystals: 1. Specimen fabrication and mechanical testing. *Journal of Geophysical Research*, *109*, B06201. https://doi.org/10.1029/2003JB002406

Jackson, I., Fitz Gerald, J. D., Faul, U. H., & Tan, B. H. (2002). Grain-size-sensitive seismic wave attenuation in polycrystalline olivine. *Journal of Geophysical Research*, *107*(B12), 2360. https://doi.org/10.1029/2001JB001225

Kamata, S., Kimura, J., Matsumoto, K., Nimmo, F., Kuramoto, K., & Namiki, N. (2016). Tidal deformation of Ganymede: Sensitivity of Love numbers on the interior structure. *Journal of Geophysical Research: Planets*, *121*, 1362–1375. https://doi.org/10.1002/2016JE005071

Karato, S.-I. (1984). Grain-size distribution and rheology of the upper mantle. *Tectonophysics*, *104*(1-2), 155–176.

Karato, S. I. (2008). *Deformation of earth materials*. Cambridge: Cambridge University Press.

Karato, S.-i. (2013). Geophysical constraints on the water content of the lunar mantle and its implications for the origin of the Moon. *Earth and Planetary Science Letters*, *384*, 144–153. https://doi.org/10.1016/j.epsl.2013.10.001

Karato, S.-i., Olugboji, T., & Park, J. (2015). Mechanisms and geologic significance of the mid-lithosphere discontinuity in the continents. *Nature Geoscience*, *8*(7), 509.

Karato, S., & Spetzler, H. A. (1990). Defect microdynamics in minerals and solid-state mechanisms of seismic wave attenuation and velocity dispersion in the mantle. *Reviews of Geophysics*, *28*(4), 399–421. https://doi.org/10.1029/RG028i004p00399

Khan, A., & Connolly, J. A. D. (2008). Constraining the composition and thermal state of Mars from inversion of geophysical data. *Journal of Geophysical Research*, *113*, E07003. https://doi.org/10.1029/2007JE002996

Khan, A., Liebske, C., Rozel, A., Rivoldini, A., Nimmo, F., Connolly, J. A. D., et al. (2018). A geophysical perspective on the bulk composition of Mars. *Journal of Geophysical Research: Planets*, *123*, 575–611. https://doi.org/10.1002/2017JE005371

Konopliv, A. S., Park, R. S., & Folkner, W. M. (2016). An improved JPL Mars gravity field and orientation from Mars orbiter and lander tracking data. *Icarus*, *274*, 253–260. https://doi.org/10.1016/j.icarus.2016.02.052

Konopliv, A. S., & Yoder, C. F. (1996). Venusian k2 tidal Love number from Magellan and PVO tracking data. *Geophysical Research Letters*, *23*(14), 1857–1860. https://doi.org/10.1029/96GL01589

Lainey, V., Dehant, V., & Pätzold, M. (2007). First numerical ephemerides of the Martian moons. *Astronomy and Astrophysics*, *465*, 1075–1084. https://doi.org/10.1051/0004-6361:20065466

Lau, H. C., & Faul, U. H. (2019). Anelasticity from seismic to tidal timescales: Theory and observations. *Earth and Planetary Science Letters*, *508*, 18–29.

Lau, H. C. P., Faul, U., Mitrovica, J. X., Al-Attar, D., Tromp, J., & Garapi, G. (2016). Anelasticity across seismic to tidal timescales: A self-consistent approach. *Geophysical Journal International*, *208*(1), 368–384. https://doi.org/10.1093/gji/ggw401

Lognonné, P. e. a. (2019). SEIS: InSight's Seismic Experiment for Internal Structure of Mars. *Space Science Reviews*, *215*(1), 12. https://doi.org/10.1007/s11214-018-0574-6

Lognonné, P., Beyneix, J. G., Banerdt, W. B., Cacho, S., Karczewski, J. F., & Morand, M. (1996). Ultra broad band seismology on InterMarsNet. *Planets and Space Science*, *44*, 1237. https://doi.org/10.1016/S0032-0633(96)00083-9

Lognonné, P., & Mosser, B. (1993). Planetary seismology. *Surveys in Geophysics*, *14*, 239–302. https://doi.org/10.1007/BF00690946

McCarthy, C., & Castillo-Rogez, J. C. (2013). Planetary ices attenuation properties, *The science of solar system ices* (pp. 183–225). New York, NY: Springer.

McCarthy, C., Takei, Y., & Hiraga, T. (2011). Experimental study of attenuation and dispersion over a broad frequency range: 2. The universal scaling of polycrystalline materials. *Journal of Geophysical Research*, *116*, B09207. https://doi.org/10.1029/2011JB008384

McSween, H. Y. Jr., & McLennan, S. M. (2014). Mars. In K. Turekian & H. Holland (Eds.), *Planets, asteriods, comets and the solar system* (pp. 251–300). Amsterdam: Elsevier Science. https://doi.org/10.1016/B978-0-08-095975-7.00125-X

Minster, J. B., & Anderson, D. L. (1981). A model of dislocation-controlled rheology for the mantle. *The Royal Society*, *299*(1449), 319–356. https://doi.org/10.1098/rsta.1981.0025

Moczo, P., & Kristek, J. (2005). On the rheological models used for time-domain methods of seismic wave propagation. *Geophysical Research Letters*, *32*, L01306. https://doi.org/10.1029/2004GL021598

Moore, W. B., & Schubert, G. (2000). NOTE: The tidal response of Europa. *Icarus*, *147*, 317–319. https://doi.org/10.1006/icar.2000.6460

Morris, S., & Jackson, I. (2009). Implications of the similarity principle relating creep and attenuation in finely grained solids. *Materials Science and Engineering: A*, *521*, 124–127.

Mosegaard, K., & Tarantola, A. (1995). Monte Carlo sampling of solutions to inverse problems. *Journal of Geophysical Research*, *100*(B7), 12,431–12,447.

Nimmo, F., & Faul, U. (2013). Dissipation at tidal and seismic frequencies in a melt-free, anhydrous Mars. *Journal of Geophysical Research: Planets*, *118*, 2558–2569. https://doi.org/10.1002/2013JE004499

Nimmo, F., Faul, U. H., & Garnero, E. J. (2012). Dissipation at tidal and seismic frequencies in a melt-free Moon. *Journal of Geophysical Research*, *117*, E09005. https://doi.org/10.1029/2012JE004160

Nowick, A. S., & Berry, B. (1972). *Anelastic relaxation in crystalline solids*. New York: Academic Press.

Padovan, S., Margot, J., Hauck, S. A., Moore, W. B., & Solomon, S. C. (2013). The tides of Mercury and possible implications for its interior structure. *Journal of Geophysical Research: Planets*, *119*, 850–866. https://doi.org/10.1002/2013JE004459

Peale, S. (1977). Rotation histories of the natural satellites. In *Iau colloq. 28: Planetary satellites*, pp. 87–111.

Peltier, W. (1974). The impulse response of a Maxwell Earth. *Reviews of Geophysics*, *12*(4), 649–669.

Plesa, A.-C., Grott, M., Tosi, N., Breuer, D., Spohn, T., & Wieczorek, M. A. (2016). How large are present-day heat flux variations across the surface of Mars? *Journal of Geophysical Research: Planets*, *121*, 2386–2403. https://doi.org/10.1002/2016JE005126

Pou, L., Mimoun, D., Lognonne, P., Garcia, R. F., Karatekin, O., Nonon-Latapie, M., & Llorca-Cejudo, R. (2018). High precision SEIS calibration for the InSight mission and its applications. *Space Science Reviews*, *215*(1), 6. https://doi.org/10.1007/s11214-018-0561-y

Qin, C., Zhong, S., & Wahr, J. (2016). Elastic tidal response of a laterally heterogeneous planet: A complete perturbation formulation. *Geophysical Journal International*, *207*(1), 89–110.

Raj, R., & Ashby, M. (1975). Intergranular fracture at elevated temperature. *Acta Metallurgica*, *23*(6), 653–666.

Ranalli, G. (2001). Mantle rheology: Radial and lateral viscosity variations inferred from microphysical creep laws. *Journal of Geodynamics*, *32*(4), 425–444. https://doi.org/10.1016/S0264-3707(01)00042-4

Remus, F., Mathis, S., Zahn, J-P, & Lainey, V. (2012). Anelastic tidal dissipation in multi-layer planets. *Astronomy & Astrophysics*, *541*, A165.

Renaud, J. P., & Henning, W. G. (2018). Increased tidal dissipation using advanced rheological models: Implications for Io and tidally active exoplanets. *The Astrophysical Journal*, *857*(2), 98.

Rivoldini, A., Van Hoolst, T., Verhoeven, O., Mocquet, A., & Dehant, V. (2011). Geodesy constraints on the interior structure and composition of Mars. *Icarus*, *213*, 451–472. https://doi.org/10.1016/j.icarus.2011.03.024

Roberts, J. H., & Nimmo, F. (2008). Tidal heating and the long-term stability of a subsurface ocean on Enceladus. *Icarus*, *194*, 675–689. https://doi.org/10.1016/j.icarus.2007.11.010

Robuchon, G., Choblet, G., Tobie, G., Čadek, O., Sotin, C., & Grasset, O. (2010). Coupling of thermal evolution and despinning of early Iapetus. *Icarus*, *207*(2), 959–971.

Rosenblatt, P., Charnoz, S., Dunseath, K. M., Terao-Dunseath, M., Trinh, A., Hyodo, R., et al. (2016). Accretion of Phobos and Deimos in an extended debris disc stirred by transient moons. *Nature Geoscience*, *9*(8), 581.

Rozel, A. (2012). Impact of grain size on the convection of terrestrial planets. *Geochemistry, Geophysics, Geosystems*, *13*, Q10020. https://doi.org/10.1029/2012GC004282

Ruedas, T., Tackley, P. J., & Solomon, S. C. (2013). Thermal and compositional evolution of the Martian mantle: Effects of phase transitions and melting. *Physics of the Earth and Planetary Interiors*, *216*, 32–58. https://doi.org/10.1016/j.pepi.2012.12.002

Sasaki, Y., Takei, Y., McCarthy, C., & Rudge, J. F. (2019). Experimental study of dislocation damping using a rock analogue. *Journal of Geophysical Research: Solid Earth*, *124*, 6523–6541. https://doi.org/10.1029/2018JB016906

Seidelmann, (P. K., Abalakin, V. K., Bursa, M., Davies, M. E., de Bergh, C., Lieske, J. H., et al. (2002). Report of the IAU/IAG working group on cartographic coordinates and rotational elements of the planets and satellites: 2000. *Celestial Mechanics and Dynamical Astronomy*, *82*(1), 83–111. https://doi.org/10.1023/A:1013939327465

Smrekar, S. E., Lognonné, P., Spohn, T., Banerdt, W. B., Breuer, D., Christensen, U., et al. (2019). Pre-mission insights on the interior of Mars. *Space Science Reviews*, *215*(1), 3.

Sohl, F., Schubert, G., & Spohn, T. (2005). Geophysical constraints on the composition and structure of the Martian interior. *Journal of Geophysical Research*, *110*, E12008. https://doi.org/10.1029/2005JE002520

Sohl, F., & Spohn, T. (1997). The interior structure of Mars: Implications from SNC meteorites. *Journal of Geophysical Research*, *102*, 1613–1636. https://doi.org/10.1029/96JE03419

Soldati, G., Boschi, L., Deschamps, F., & Giardini, D. (2009). Inferring radial models of mantle viscosity from gravity (GRACE) data and an evolutionary algorithm. *Physics of the Earth and Planetary Interiors*, *176*, 19–32. https://doi.org/10.1016/j.pepi.2009.03.013

Stevenson, D. J. (2001). Mars' core and magnetism. *Nature*, *412*, 214–219.

Stewart, A. J., Schmidt, M. W., van Westrenen, W., & Liebske, C. (2007). Mars: a new core-crystallization regime. *Science*, *316*, 1323. https://doi.org/10.1126/science.1140549

Stixrude, L., & Lithgow-Bertelloni, C. (2005b). Mineralogy and elasticity of the oceanic upper mantle: Origin of the low-velocity zone. *Journal of Geophysical Research*, *110*, B03204. https://doi.org/10.1029/2004JB002965

Stixrude, L., & Lithgow-Bertelloni, C. (2011). Thermodynamics of mantle minerals—II. Phase equilibria. *Geophysical Journal International*, *184*, 1180–1213. https://doi.org/10.1111/j.1365-246X.2010.04890.x

Sundberg, M., & Cooper, R. (2010). A composite viscoelastic model for incorporating grain boundary sliding and transient diffusion creep; correlating creep and attenuation responses for materials with a fine grain size. *Philosophical Magazine*, *90*(20), 2817–2840. https://doi.org/10.1080/14786431003746656

Takei, Y. (2017). Effects of partial melting on seismic velocity and attenuation: A new insight from experiments. *Annual Review of Earth and Planetary Sciences*, *45*(1), 447–470. https://doi.org/10.1146/annurev-earth-063016-015820

Takei, Y., Karasawa, F., & Yamauchi, H. (2014). Temperature, grain size, and chemical controls on polycrystal anelasticity over a broad frequency range extending into the seismic range. *Journal of Geophysical Research: Solid Earth*, *119*, 5414–5443. https://doi.org/10.1002/2014JB011146

Taylor, G. J. (2013). The bulk composition of Mars. *Chemie Der Erde-Geochemistry*, *73*(4), 401–420.

Taylor, S. R., & McLennan, S. (2008). *Planetary crusts: Their composition, origin and evolution*, *Cambridge Planetary Science*. Cambridge: Cambridge University Press. https://doi.org/10.1017/CBO9780511575358

Tromp, J., & Mitrovica, J. X. (1999). Surface loading of a viscoelastic Earth—I. General theory. *Geophysical Journal International*, *137*, 847–855. https://doi.org/10.1046/j.1365-246X.1999.00838.x

Van Hoolst, T., Dehant, V., Roosbeek, F., & Lognonné, P. (2003). Tidally induced surface displacements, external potential variations, and gravity variations on Mars. *Icarus*, *161*, 281–296. https://doi.org/10.1016/S0019-1035(02)00045-3 van Thienen, P., Rivoldini, A., Van Hoolst, T., & Lognonné, P. (2006). A top-down origin for Martian mantle plumes. *Icarus*, *185*, 197–210. https://doi.org/10.1016/j.icarus.2006.06.008

Wahr, J., Selvans, Z. A., Mullen, M. E., Barr, A. C., Collins, G. C., Selvans, M. M., & Pappalardo, R. T. (2009). Modeling stresses on satellites due to nonsynchronous rotation and orbital eccentricity using gravitational potential theory. *Icarus*, *200*, 188–206. https://doi.org/10.1016/j.icarus.2008.11.002

Williams, J. G., & Boggs, D. H. (2015). Tides on the Moon: Theory and determination of dissipation. *Journal of Geophysical Research: Planets*, *120*, 689–724. https://doi.org/10.1002/2014JE004755

Williams, J. G., Konopliv, A. S., Boggs, D. H., Park, R. S., Yuan, D.-N., Lemoine, F. G., et al. (2014). Lunar interior properties from the GRAIL mission. *Journal of Geophysical Research: Planets*, *119*, 1546–1578. https://doi.org/10.1002/2013JE004559

Williams, J. G., Turyshev, S. G., Boggs, D. H., & Ratcliff, J. T. (2006). Lunar laser ranging science: Gravitational physics and lunar interior and geodesy. *Advances in Space Research*, *37*(1), 67–71.

Yoder, C. F. (1995). Venus' free obliquity. *Icarus*, *117*(2), 250–286.

Yoder, C. F., Konopliv, A. S., Yuan, D. N., Standish, E. M., & Folkner, W. M. (2003). Fluid core size of Mars from detection of the solar tide. *Science*, *300*, 299–303. https://doi.org/10.1126/science.1079645

Zharkov, V. N., & Gudkova, T. V. (1997). On the dissipative factor of the Martian interiors. *Planets and Space Science*, *45*, 401–407. https://doi.org/10.1016/S0032-0633(96)00144-4

Zharkov, V. N., & Gudkova, T. V. (2005). Construction of Martian interior model. *Solar System Research*, *39*, 343–373. https://doi.org/10.1007/s11208-005-0049-7

Zharkov, V. N., & Gudkova, T. V. (2009). The period and *Q* of the Chandler wobble of Mars. *Planss*, *57*, 288–295. https://doi.org/10.1016/j.pss.2008.11.010

Erratum

In the originally published version of this paper, Figure 10 was incorrect. This error has since been corrected and this version may be considered the authoritative version of record.